Golgins support extracellular matrix secretion by collectively maintaining the Golgi structure-function relationship

Condensed title: Golgins support extracellular matrix secretion

George Thompson[1], Anna Hoyle[2,3,4], Philip A. Lewis[5], M. Esther Prada-Sanchez[1], Joe Swift[2,3], Kate Heesom[5], Martin Lowe[6], David Stephens[1], Nicola Stevenson[1†]

[†] Corresponding author: nicola.stevenson@bristol.ac.uk

[1] School of Biochemistry, University of Bristol, Biomedical Sciences Building, University Walk, Bristol, BS8 1TD.

[2] Wellcome Centre for Cell-Matrix Research, Oxford Road, Manchester, M13 9PT, UK

[3] Division of Cell Matrix Biology and Regenerative Medicine, School of Biological Sciences, Faculty of Biology, Medicine and Health, Manchester Academic Health Science Centre, University of Manchester, Manchester, M13 9PL, UK

[4] Current address: Kennedy Institute of Rheumatology, University of Oxford, Oxford, OX3 7FY, UK

[5] Proteomics facility, University of Bristol, Biomedical Sciences Building, University Walk, Bristol, BS8 1TD

[6] School of Biological Sciences, Faculty of Biology, Medicine and Health, University of Manchester, The Michael Smith Building, Oxford Road, Manchester, M13 9PT, UK

ORCID IDS:

George Thompson: https://orcid.org/0000-0003-4511-4194
Anna Hoyle: https://orcid.org/0000-0002-6517-2546
Philip Lewis: https://orcid.org/0000-0002-2868-2459
M. Esther Prada-Sanchez: https://orcid.org/0000-0003-0118-7586
Joe Swift: https://orcid.org/0000-0002-5039-9094
Kate Heesom: https://orcid.org/0000-0002-5418-5392
Martin Lowe: https://orcid.org/0000-0002-9331-8143
David Stephens: https://orcid.org/0000-0001-5297-3240
Nicola Stevenson: https://orcid.org/0000-0001-8967-7277

Abstract

The secretion of extracellular matrix (ECM) proteins is vital to the maintenance of tissue health. One major control point of this process is the Golgi apparatus, whose dysfunction causes numerous connective tissue disorders. Golgi function is tightly linked to its structure, which is maintained by the cytoskeleton and Golgi organising proteins. We sought to investigate the role of two of these organising proteins, the golgins GMAP210 and Golgin-160, in ECM secretion. We found that loss of either protein had distinct impacts on Golgi organisation. GMAP210 loss caused cisternal fragmentation and dilation, alongside the accumulation of tubulovesicular structures. Meanwhile, Golgin-160 knockout lead to Golgi fragmentation and vesicle build-up. Nonetheless, loss of each protein had a similar impact on ECM secretion and glycosaminoglycan synthesis. We therefore propose that golgins are collectively required to create the correct physical-chemical space to support efficient ECM protein secretion and modification. This is the first time that Golgin-160 has been shown to be required for ECM secretion.

Summary

In this study, Thompson *et al* demonstrate that two cis-Golgi golgins, GMAP210 and Golgin-160, have distinct, non-redundant roles in maintaining Golgi organisation and that both are required to support the efficient secretion, assembly, and modification of extracellular matrix proteins.

Introduction

The extracellular matrix (ECM) is a complex network of proteins, carbohydrate and mineral secreted by cells to build a scaffold that forms the structural basis of most tissues. To date, current resources describing the 'matrisome' have identified >1000 proteins associated with this compartment in humans (Shao et al., 2023), explaining the capacity for extensive diversification of biochemical and mechanical properties between tissue types. The most abundant family of ECM proteins are the collagens. These proteins assemble to form the main structural components of connective tissues alongside other fibre and network forming proteins such as fibronectin and elastin (Karamanos et al., 2021). This assembly is supported by accessory factors like the proteoglycans (Couchman and Pataki, 2012), a diverse set of proteins characterised by the presence of at least one glycosaminoglycan (GAG) chain which helps to promote tissue hydration and sequester signalling molecules (Gandhi and Mancera, 2008). Meanwhile ECM turnover is regulated by secreted proteases (Arpino et al., 2015; Lee and Murphy, 2004).

All newly synthesized ECM proteins must transit the secretory pathway to reach the extracellular environment for assembly. As they do so, many are heavily modified, which alters their chemistry and consequently the way in which they interact and assemble (Adams, 2023). Regulation of ECM protein modification is therefore crucial to the assembly of a functional matrix. One of the main compartments responsible for facilitating this process is the Golgi apparatus, which contains enzymes catalysing modifications such as O-glycosylation, N- and O-linked glycan maturation, proteolytic processing, phosphorylation, lipidation and sulphation (Potelle et al., 2015). Given this central role in protein processing it is unsurprising that a great number of genes affecting Golgi function have been linked to various connective tissue disorders (Hellicar et al., 2022).

Golgi structure is highly complex and tightly linked to its function. In mammalian systems it is composed of a stack of flattened, fenestrated membranous compartments called cisternae, which are laterally connected to form an interconnected Golgi ribbon (Lowe, 2011). These stacks are polarised such that cargoes arriving from the ER enter the Golgi stack at the *cis*-face, transit through the *medial* and *trans* compartments, and then get sorted before exiting the Golgi at the *trans* Golgi network (TGN). Golgi resident enzymes are distributed across the cisternae with a *cis-trans* polarity to support the successive addition of post-translational modifications to cargoes as they transit the compartments (Rabouille et al., 1995; Tie et al., 2022). This distribution is maintained by intra-Golgi vesicular transport which recycles enzymes between Golgi cisternae (Arab et al., 2024).

One of the major protein families responsible for maintaining Golgi organisation is the golgin family (Barr and Short, 2003; Gillingham and Munro, 2016; Witkos and Lowe, 2015). These proteins project coiled-coil domains into the cytosol from the Golgi surface to tether other Golgi membranes and transport vesicles (Lowe, 2019; Wong and Munro, 2014). Specific golgins localise to distinct regions of the Golgi organelle and this, combined with their affinity for different vesicles, confers

directionality and specificity to intra-Golgi traffic (Wong et al., 2017). We and others have shown that one of these golgins, giantin, is required for the secretion of a healthy extracellular matrix. Loss of giantin prevents proper processing of the procollagen type I N-propeptide (Stevenson et al., 2021), impacts the abundance of ECM proteins (Katayama et al., 2018; Kikukawa and Suzuki, 1992), and impairs GAG metabolism (Kikukawa et al., 1991a; Kikukawa et al., 1991b; Kikukawa et al., 1990). These phenotypes are variable between animal models, but interestingly, always impact skeletal development (Katayama et al., 2011; Lan et al., 2016; Stevenson et al., 2017; Suzuki et al., 1988).

Another golgin which has been linked to ECM deposition and skeletal development is GMAP210. Mutations in the *TRIP11* gene encoding GMAP210 are causative of the human skeletal diseases achondrogenesis type 1A and odontochondrodysplasia (Costantini et al., 2021; Del Pino et al., 2021; Medina et al., 2020; Qian et al., 2021; Smits et al., 2010; Upadhyai et al., 2021; Wehrle et al., 2019; Yeter et al., 2022). Interestingly, *Trip11* mutant mice have a similar phenotype to giantin mutant rats, with both models showing neonatal lethal chondrodysplasia characterised by craniofacial defects, shortened limbs and ribs, and delayed mineralisation of bone (Bird et al., 2018; Follit et al., 2008; Smits et al., 2010; Yamaguchi et al., 2021). Loss of GMAP210 also impacts the secretion of specific ECM proteins in a selective manner (Bird et al., 2018; Smits et al., 2010; Yamaguchi et al., 2021)

Altogether these studies suggest that extracellular matrix secretion is particularly susceptible to the loss of at least two golgins, which appear to act non-redundantly in this context. This led us to question the extent to which ECM deposition is sensitive to the loss of golgins more widely, and how this relates to changes in Golgi organisation. To begin addressing this, we performed a comparative study between GMAP210 and a third golgin, Golgin-160. Golgin-160 was chosen because it resides on *cis*-Golgi membranes like GMAP210 (Hicks et al., 2006) but remains poorly characterised at a functional level. Here we report that knockout of Golgin-160 has a similar impact on ECM organisation and composition as GMAP210 loss. Golgi morphology on the other hand, is affected differently, consistent with the two golgins acting in different ways to maintain Golgi homeostasis. We therefore conclude that GMAP210 and Golgin-160 function non-redundantly to create the correct physical and biochemical space to support the modification and secretion of complex ECM molecules.

Results

Generation of golgin knockout cell lines

To test the role of different golgins on matrix secretion, we generated two GMAP210 and Golgin-160 knockout (KO) clones using CRISPR-Cas9 genome engineering. GMAP210 KO clone 1 was generated using a gRNA targeting exon 4 of the *TRIP11* gene (Supplemental Figure 1A). This exon is common to both predicted protein coding transcripts TRIP11-201 (Ensembl transcript ID ENST00000267622.8 Uniprot ID Q15643-1) and TRIP11-202 (ENST00000554357.5, H0YJ97) and so mutation should impact all protein expression. The generated mutation was a single base pair insertion of alanine resulting in a frame shift from position Glu^{114} and truncation at amino acid 155 (Supplemental Figure 1A). GMAP210 KO clone 2 was generated using a gRNA targeting exon 1 of transcript TRIP11-202 and upstream of the predicted start site of the longer transcript TRIP11-201. This resulted in a 10bp deletion in the promoter region (Supplemental Figure 1A). Loss of protein expression was confirmed in both clones by immunofluorescence using three different antibodies targeting the N- and C-terminus of the GMAP210 protein (Supplemental Figure 1B) and western blotting (Supplemental

Figure 1C). Note trance amounts of protein could be detected with the C-terminal antibody suggesting a truncation product may persist. Nonetheless, we considered this sufficient depletion for further study.

Golgin-160 KO clones were generated using a gRNA targeting exon 20 of transcript GOLGA3-201 (ensemble ID ENST00000204726.9, Uniprot ID: Q08378-1). This is expected to mutate all predicted transcripts encoding fragments larger than 44 amino acids. Mutation with this gRNA consistently produced a single alanine insertion, resulting in frame shift at amino acid Glu^{1312} and truncation at amino acid 1331 (Supplemental Figure 1A). Consequently, two clones with the same mutation were carried forward for experiments to rule out clonal effects. Protein loss was confirmed by immunofluorescence and western blotting, again with antibodies targeting both the N- and C-terminus (Supplemental Figure 1D,E).

Loss of either GMAP210 or Golgin-160 causes changes in ECM assembly and organisation

To investigate the requirement for GMAP210 and Golgin-160 in ECM secretion and assembly, we grew our new KO lines for a week in the presence of ascorbic acid to promote collagen secretion and visualised the cell-derived ECM by immuno-fluorescence labelling. Co-labelling of two major fibrillar ECM components, collagen type 1 and fibronectin, revealed an extensive network of highly aligned and organised extracellular fibrils in wildtype (WT) cell cultures, with cell nuclei stretching along the fibril axis (Figure 1A-D). In GMAP210 (Figure 1A-B) and Golgin-160 KO (Figure 1C-D) cell cultures on the other hand, fibrils were identifiable, but they were less well ordered, showing poor alignment and an increase in branching. To examine the structure of these fibrils more closely, the cell layer was extracted, and the remaining cell-derived matrix was imaged by high-speed atomic force microscopy (HS-AFM). Again, fibrils were less well organised in all golgin KO cultures (Figure 1E-F). They were also thinner, however the periodicity of the collagen fibrils was largely unchanged, suggesting assembly of collagen trimers into fibrils is normal but lateral interconnections between fibrils may be reduced.

The overall fluorescence intensity of collagen staining in the matrix appeared reduced in the KO cultures. We therefore determined the abundance of collagen type I in lysate and matrix fractions of cell cultures by immunoblotting against the Col1a1 chain. Col1a1 abundance in the lysate fractions of mutant cultures was comparable to that of WT lysates when normalised to total protein, suggesting expression is normal and collagen is not retained inside the cell (Figure 2A,Ci). Col1a1 abundance was, however, reduced in the ECM fraction of all mutant lines when normalised against total cellular protein (Figure 2B, Cii), suggesting it is not being efficiently incorporated into the insoluble matrix. Collagen in the media was below the level of detection by this method.

ECM composition is altered following loss of GMAP210 and Golgin-160

To determine whether the observed changes in ECM organisation in the golgin KO cultures reflect changes in ECM composition, the cell-derived matrix from WT and KO cultures was collected and analysed by mass-spectrometry. Principal component analysis showed distinction between the WT and Golgin-160 KO and between the KO matrix samples, but variation between repeats was high (Supplementary Figure2A). Results were filtered against the matrisome database (Shao et al., 2023) to indicate proteins specifically related to ECM structure and function. Overall, fewer proteins were significantly impacted by loss of Golgin-160 than of GMAP210, however there was a great deal of overlap between the KO lines (Figure 3). For example, laminin subunit gamma 1 (LAMC1), Laminin subunit alpha 5 (LAMA5), hemicentin-1 (HMCN1), Latent Transforming Growth Factor Beta Binding

165 Protein 1 (LTBP1) and Transforming Growth Factor Beta 2 (TGFB2) were significantly reduced in
166 abundance in at least one Golgin-160 KO line as well as the GMAP210 KOs (Figure 3A-C). Conversely,
167 the abundance of fibrillins was increased in all KO lines (Figure 3A-C). Interestingly, Lysyl Oxidase Like
168 1 (LOXL1), which was upregulated in the GMAP210 KO ECM, was downregulated in Golgin-160 KOs,
169 and vice versa for Procollagen-Lysine,2-Oxoglutarate 5-Dioxygenase 1 (PLOD1, Figure 3A-C). This hints
170 at golgin specific changes in the post-translational modification of collagen. Altogether these data
171 show that both GMAP210 and Golgin-160 are required for the deposition of a well-organised ECM.
172 The similarity seen between ECM phenotypes in GMAP210 and Golgin-160 KO cells also
173 demonstrates the non-redundant nature of these golgins in this context and the broad susceptibility
174 of ECM cargoes to golgin loss.

175 *GMAP210 and Golgin-160 are not required for procollagen processing*

176 We have shown previously that KO of giantin disrupts procollagen processing (Stevenson et al.,
177 2021). To test whether impaired collagen processing is contributing to the ECM phenotypes reported
178 here too, we interrogated our ECM proteomics data set for peptides relating to collagen pro-
179 domains. Collagen type IV had the highest peptide count and therefore provided the most robust
180 analysis. Comparing the average peptide counts across the Col4a2 sequence we found no significant
181 increase in the number of peptides containing an intact N-propeptide cleavage site in the KO cultures
182 (N-propeptide overlap sequence, Supplemental Figure 2B and C), indicating that processing of
183 collagen type IV proceeds effectively in the absence of Golgin-160 and GMAP210. Expression of a
184 procollagen type 1 construct in which the N-propeptide is GFP tagged (McCaughey et al., 2019), also
185 revealed the presence of free collagen type I N-propeptide cleavage products in both WT and Golgin-
186 160 KO cells indicating successful cleavage (Supplemental Figure 2D). GMAP210 KO cells did not
187 tolerate procollagen type I over-expression and could not be tested. Altogether, these data indicate
188 that loss of GMAP210 or Golgin-160 does not phenocopy loss of giantin with respect to collagen
189 processing, and that this is not a contributing factor to the observed ECM phenotypes here.

190 *Loss of GMAP210 or Golgin-160 leads to distinct changes in Golgi morphology*

191 Having established that loss of GMAP210 or Golgin-160 has a similar impact on ECM deposition, we
192 next sought to determine the impact of golgin loss on Golgi organisation. Cells were labelled with
193 markers of the *cis*- and *medial*-Golgi and the *trans*-Golgi network (TGN). Golgi area and extent of
194 fragmentation were then measured (Figure 4A-D). Strikingly, each golgin KO had a different impact
195 on Golgi morphology. As previously reported (Bird et al., 2018; Sato et al., 2015; Smits et al., 2010;
196 Wehrle et al., 2019; Yamaguchi et al., 2022), loss of GMAP210 resulted in a clear compaction of Golgi
197 structures compared to wildtype cells (Figure 4A-B). The Golgi also appeared fragmented, although
198 this was difficult to quantify due to this compaction and poor definition of Golgi elements. In Golgin-
199 160 KO cells on the other hand, no consistent change in Golgi size was observed, but there was a
200 clear increase in Golgi fragment number (Figure 4C-D). In all KO lines, the *cis-trans* polarity of the
201 Golgi appeared to be maintained, although again this was harder to ascertain in the GMAP210 KO
202 cells (Figure 4A, C).

203 To better define the impact of KO on Golgi membrane organisation, higher resolution imaging was
204 performed using single-tilt electron tomography. For each cell line, 3D tomographic reconstructions
205 were generated (Supplemental movies 1-3) and a section of the Golgi was segmented to build a 3D
206 model of membrane organisation (Supplemental movies 1-3, Figure 4E-G). In these models,

207 membranes associated with the Golgi apparatus were grouped into four structural categories:
208 cisternae (blue), defined as laterally flattened, stacked membranous compartments; dilated
209 structures (red) - large volume structures lacking flattened regions; tubulovesicular structures
210 (yellow) - convoluted structures with interconnected regions of spherical and tubular shape; and
211 vesicles (green) – small, spherical structures.

212 In wildtype cells, as expected, we observed tightly stacked, evenly flattened, fenestrated cisternae
213 that were laterally connected to span lengths of tens of microns (Figure 4E). Dilated and
214 tubulovesicular structures were predominantly localised to the *trans* side of the Golgi in these cells,
215 with small numbers of vesicles concentrated at the cisternal rims and *trans*-Golgi face. In contrast,
216 although the Golgi was identifiable in GMAP210 KO cells, membranes were highly disordered (Figure
217 4F). The cisternae were mostly stacked, but they were short with no lateral connections and few
218 fenestrations, and many were dilated or had bulges along their length, particularly at the *cis*- and
219 *trans*- end of the stack. Some membranous structures resembling these dilated cisternae were also
220 observed near, but not part of, a stack but their origin and identity is hard to assign. Finally, in many
221 instances the cisternae were surrounded by extensive tubulovesicular structures interspersed with
222 vesicles that wrapped around the mini-stacks (Figure 4Fiii, iv). Some of these structures had tunnel
223 like indentations, which in cross-section appeared as internalised vesicles but were continuous with
224 the cytosol (Figure 4Fii-iii, open headed arrows). Note, we did not see any obvious ER swelling as has
225 been reported to occur in a cell type specific manner in some *in vivo* studies (Bird et al., 2018; Smits
226 et al., 2010; Yamaguchi et al., 2021). Despite the similarity of the tubulovesicular membranes to
227 ERGIC membranes (Appenzeller-Herzog and Hauri, 2006), we did not see any gross changes to
228 ERGIC53 distribution in these cells at the light level (Supplementary Figure 3A). To conclude, the
229 geometry and organisation of Golgi membrane is severely perturbed in the absence of GMAP210 in a
230 way that is suggestive of both structural and trafficking defects.

231 Examination of Golgin-160 KO cells showed well stacked, tightly flattened cisternae that remained
232 juxtanuclear as in wildtype cells (Figure 4G). However, consistent with the immunofluorescence data,
233 there were very few lateral connections between cisternae meaning membranes were fragmented
234 into closely apposed ministacks rather than forming a classical ribbon architecture (Figure 4Gi, pink
235 brackets). Cisternae also appeared to have internal vesicles or holes unlike control cells (Figure 4Gii,
236 double headed arrows). Strikingly, there was a clear accumulation of vesicular structures in the area
237 surrounding the cisternal rims, as well as both the *cis*- and *trans*-Golgi face (Figure 4Gv). This
238 coincided with a high incidence of spherical structures attached to the membranes of cisternal rims
239 that resembled frustrated vesicle budding or fusion profiles (Figure 4Gii, pink arrow). Intriguingly,
240 budding vesicles were also frequently observed at the nuclear envelope (Figure 4Giii, closed head
241 arrows). Although the accumulating vesicles were reminiscent of COPI vesicles with an electron
242 dense coat, we were unable to observe any gross changes in COPI localisation at the light level by
243 immunofluorescence and individual puncta could not be distinguished in the Golgi region
244 (Supplemental Figure 3B). In conclusion, loss of GMAP210 or Golgin-160 has a different impact on
245 Golgi structural organisation.

246 *Loss of either GMAP210 or Golgin-160 leads to reduced secretion of ECM components and regulators*

247 Given the clear disruption to Golgi organisation in our knockout lines, we decided to look at secretion
248 more generally. Cells were grown in serum-free medium overnight, before collecting the media to
249 analyse the abundance of soluble secreted proteins by mass spectrometry. Three independent

250 replicate samples were collected for all WT and KO lines and analysed simultaneously by 15-plex
251 tandem-mass tagging mass spectrometry. The sum of raw abundance revealed replicate one to have
252 contained more protein and thus pair-wise comparisons within replicates were chosen over averages
253 (Supplemental Figure 4A). Principal component analysis reiterated the need for paired analysis with
254 PC1 and 2 separating the samples by replicate, however good separation was observed at PC3 and
255 PC4 between WT, Golgin-160 KO and GMAP210 KO lines, with individual clones clustering together
256 for each KO. This indicates genotype is a key contributor to variance and highlights variation between
257 secretomes in each line (Supplemental Figure 4B). The two individual KO clones for each golgin were
258 pooled using a linear regression model to increase statistical power. Log-fold change in protein
259 abundance was plotted against p-value to identify proteins whose secretion is significantly altered in
260 KO cultures compared to WT (Figure 5).

261 In total, 482 proteins and 427 proteins showed altered raw abundance ($p<0.05$) in the secretome of
262 GMAP210 KO and Golgin-160 KO cultures respectively compared to wild-type cells (Figure 5A,
263 Supplemental Figure 4C). GO term analysis revealed that the top 15 biological pathways affected in
264 both golgin KO samples included collagen fibril and extracellular matrix organisation, consistent with
265 the ECM defects described above, as well as cell adhesion and migration (Supplemental Table 1).
266 Proteins involved in osteoblast and chondrocyte differentiation were also impacted by golgin loss.
267 This was not surprising for the GMAP210 KOs given the skeletal phenotypes reported in animal
268 models and human disease (Bird et al., 2018; Costantini et al., 2021; Del Pino et al., 2021; Follit et al.,
269 2008; Medina et al., 2020; Qian et al., 2021; Smits et al., 2010; Upadhyai et al., 2021; Wehrle et al.,
270 2019; Yamaguchi et al., 2021), but intriguingly, a similar effect was seen following loss of Golgin-160,
271 which has not been reported to cause a skeletal phenotype in mice (Banu et al., 2002; Bentson et al.,
272 2013). Pathways associated with proteolysis and signalling appeared to be impacted by the loss of
273 Golgin-160 specifically (Supplemental Table 1).

274 Examination of the individual proteins most heavily affected by loss of each golgin shows a clear
275 depletion of ECM components and regulators in the media of both KO cultures, with a high degree of
276 overlap between GMAP210 and Golgin-160 KOs (Figure 5A - proteins impacted in the same way by
277 each KO circled blue, Supplemental Figure 4C). For example, the protein family showing the greatest
278 depletion in both mutant media fractions were the proteoglycans. Biglycan (BGN), decorin (DCN),
279 versican (VCAN) all showed reduced abundance in both KO samples, with aggrecan (AGRN) also
280 depleted in the Golgin-160 KO and testican (SPOCK1) impacted in the GMAP210 KOs. This suggests
281 the proteoglycans are particularly susceptible to Golgi dysfunction (Figure 5A – proteins in green).
282 Collagen types IV, V and VI, fibronectin (FBN), and nidogen 2 (NID2) also showed reduced abundance
283 in the media from both KO lines compared to WT (Figure 4A). Similarly, the secretion of matrix
284 regulating enzymes such as FAM20C Golgi Associated Secretory Pathway Kinase (FAM20C) and
285 PLOD2, as well as signalling molecules like TGFb, Growth Differentiation Factor 6 (GDF6) and LTBP2,
286 was significantly downregulated in both KOs. Surprisingly, the protein showing the greatest increase
287 in secretion in both KO lines was the intracellular protein Rho GDP Dissociation Inhibitor Beta
288 (ARHGDIB), indicating aberrant translocation to the extracellular space.

289 As well as these similarities, we also observed many golgin-specific changes in this data set (Figure
290 5A - proteins circled in purple differentially impacted by each KO, Supplemental Figure 4C). For
291 instance, thrombospondin secretion is more greatly affected in GMAP210 KO cultures, whilst Golgin-
292 160 KO cells fail to efficiently secrete numerous additional ECM proteins and regulators like laminins

293 and TIMP metalloproteases. Several components of the complement system also showed reduced
294 secretion in the Golgin-160 KO cell lines implying this pathway may be impaired following Golgin-160
295 loss (Figure 5Aii and Supplemental Figure 4C). Overall, most proteins impacted by Golgin-160 loss
296 showed reduced rather than increased abundance in culture media. In GMAP210 KO cells on the
297 other hand, there were a significant number of proteins showing increased secretion, although these
298 tended not to be ECM components. Of note, several lysosomal enzymes were released from
299 GMAP210 KO cells suggesting either poor sorting at the Golgi or increased lysosome secretion
300 (Figure 5Aii and Supplemental Figure 4C). In conclusion, although the secretion of a large subset of
301 ECM proteins is broadly susceptible to loss of golgin function, there are also cargoes that show
302 specificity with respect to their reliance on particular golgins.

303 *Golgin KOs induce changes in gene expression for some secreted proteins*

304 Changes in secreted protein abundance in cell culture medium could arise due to altered gene
305 expression of the cargos or altered trafficking to the cell surface. To test the former, we performed
306 RT-PCR to measure the expression of cargo proteins identified in the secretome analysis. The
307 proteins showing the greatest negative and positive fold change in abundance in the media of the KO
308 cells were biglycan and ARHGDIB respectively. Consistent with this, we found that the expression of
309 mRNA encoding each protein mirrored these changes, with biglycan expression reduced and
310 ARHGDIB expression increased in KO clones (Figure 5B,C). To determine whether gene expression
311 correlated with secretion more widely, three more targets were tested by RT-PCR: THBS1, which is
312 only affected in GMAP210 KO cells; PLOD1, which is only impacted by Golgin-160 loss; and FAM20C,
313 which shows reduced secretion in both KO lines. The expression of FAM20C was reduced in all KO
314 clones, in line with secretion (Figure 5D). However, PLOD1 expression was not significantly altered in
315 any of the KO lines (Figure 5E) and THBS1 expression was not consistently impacted (Figure 5F). Gene
316 expression levels therefore did not fully predict secretion patterns for all targets, suggesting golgin
317 loss can lead to changes to ECM secretion in different ways.

318 *Biglycan trafficking is unaffected by golgin loss*

319 We next wanted to determine the direct impact of our golgin mutations on cargo transport and
320 modification. For this we focused on biglycan as the protein showing the greatest fold change in
321 secretion in all lines. Stable cell lines were generated expressing a construct encoding biglycan
322 tagged with both mScarlet and a streptavidin binding protein (SBP) to allow live imaging of
323 exogenous biglycan transport under the control of the RUSH trafficking system (Boncompain et al.,
324 2021). In this system, tagged biglycan is expressed alongside a streptavidin-tagged ER hook, which
325 binds the SBP tag on the biglycan and holds it in the ER. The addition of biotin prior to imaging is
326 then used to outcompete this interaction and release biglycan for anterograde trafficking. In these
327 experiments, the ER hook (not fluorescently labelled) is transiently expressed on a bi-cistronic vector
328 that also encodes BFP-tagged Mannosidase-II (MannII-BFP) to provide a Golgi marker.

329 In the absence of ER hook, stably expressed BGN-SBP-mSc was localised to both the ER and Golgi in
330 all cell lines (Supplemental Figure 5). After transient transfection with the ER hook, successful
331 anchoring of the tagged biglycan was confirmed by localisation of fluorescence to the ER at steady
332 state (Figure 6Ai, Bi, Ci T 00:00). Upon the addition of biotin, biglycan began to accumulate in
333 cytoplasmic punctae, presumed to be ER exit sites, before moving towards the Golgi region in
334 punctate carriers (Supplemental Movies 4-6, Figure 6Aii, Bii, Cii). Arrival at the Golgi region occurred

335 approximately 14 minutes after biotin addition in all cases (Figure 6D). Here, the biglycan signal
336 initially accumulated adjacent to the ManII-BFP labelled structures, but then showed increasing
337 colocalization with ManII-BFP as it progressed through the stack (Supplemental Movies 4-6, Figure
338 6Ai, Bi, Ci). Finally, approximately 20 minutes after arrival at the Golgi, the emergence of post-Golgi
339 carriers carrying biglycan to the cell periphery was readily observed (Figure 6Aiii, Biii, Ciii, E). Overall,
340 transport kinetics were similar in all lines tested (Figure 6D,E), suggesting biglycan secretion is
341 unimpeded by loss of GMAP210 or Golgin-160, at least in an over-expression bulk transport system.
342 The changes in Golgi organisation observed in KO lines do not therefore significantly impact general
343 cargo transport.

344 *Post-translational modification of biglycan is impaired in golgin KO cell lines*

345 The inter-connectivity of Golgi cisternae and their spatial organisation is important to support and
346 optimise the function of Golgi resident enzymes that post-translationally modify cargoes (Zhang and
347 Wang, 2016). ECM proteins are often highly modified and these modifications are important to their
348 assembly (Adams, 2023). We therefore sought to determine whether the disruption to Golgi
349 organisation in our mutants impacts ECM protein modification, which may in turn contribute to
350 assembly defects. Proteoglycans are heavily modified by the addition of large, sulphated GAG chains,
351 making them highly susceptible to Golgi dysfunction. We therefore continued to focus on biglycan as
352 a model cargo.

353 To look for changes in modification, cells stably expressing BGN-SBP-mSc were grown in serum free
354 media overnight before collecting the media and lysate fractions of cultures for western blotting.
355 Immunoblotting for both biglycan and the mScarlet tag showed that exogenous biglycan is secreted
356 by all mutant lines (Figure 7A), consistent with the RUSH assays. Furthermore, the ratio of
357 intracellular to extracellular protein was maintained, suggesting secretion rates are similar (Figure
358 7B). We did, however notice a shift in the molecular weight distribution of secreted biglycan in
359 mutant cultures. In WT conditioned media, secreted BGN-SBP-mSc was identifiable as a broad band
360 at around 250 kDa, with a small amount of protein running at 150kDa. In all KO lines however, a
361 higher proportion of the protein ran at the lower molecular weight (Figure 7A). Calculation of the
362 normalised ratio of 250 kDa vs 150 kDa protein confirmed this observation (Figure 7C). Blotting with
363 the higher affinity RFP antibody also showed the presence of fully unmodified BGN-SBP-mSc at
364 75kDa in the media fraction, which was again secreted to a greater extent by KO cells (Figure 7A).
365 These data suggest biglycan post-translational modification is perturbed in a similar way in the
366 absence of either golgin.

367 To better understand the nature of the biglycan modification defect, we first assessed N-glycosylation
368 by subjecting secreted BGN-SBP-mSc to digestion by PNGase F, which cleaves N-glycan chains. After
369 treatment, an identical small shift in biglycan molecular weight was observed in all samples
370 indicating that this modification is intact in KO cultures (Figure 7D). Note, digestion had little impact
371 on the higher molecular weight bands suggesting N-glycosylation does not contribute a significant
372 amount to the mass of these biglycan forms. On the other hand, treatment of immunoprecipitated
373 biglycan with chondroitinase ABC which digests GAG chains, did result in the loss of all higher and
374 mid-molecular weight forms (Figure 7E). Interestingly, there was some resistance to digest in the
375 GMAP210 KO clones that we attribute to altered modifications affecting enzyme-substrate affinity.
376 Thus, we conclude that glycanation of biglycan is defective in the golgin KO cells.

One Golgi organisational feature common to both GMAP210 and Golgin-160 KO lines is fragmentation of the Golgi ribbon. To test if this would be sufficient to impair GAG chain synthesis, we fragmented the Golgi in our cell lines using the microtubule depolymerising agent nocodazole and repeated our secretion assays. Consistent with other studies (Harada et al., 2024), drug treatment impaired BGN modification in WT cells (Figure 7F). Surprisingly however, we also found that nocodazole treatment exacerbated the GAG modification defects in mutant cells, suggesting the observed fragmentation in KO lines was not fully pervasive. Overall, our studies show that GAG chain synthesis is impaired in the absence of both golgins tested.

Discussion

In this study we show that loss of two *cis*-Golgi localised golgins causes distinct changes to Golgi morphology and function that ultimately lead to similar defects in ECM secretion, assembly and organisation. This is the first time that loss of Golgin-160 has been shown to impact ECM deposition and highlights the broad susceptibility of ECM cargoes to golgin loss. Altogether our data suggest that the impact of golgin depletion on ECM assembly is manifold, with gene expression, protein secretion, protein modification and ECM turnover all affected.

This study provides the most in-depth characterisation of Golgi structure in the absence of GMAP210 to date. In agreement with previous reports, we observed that loss of GMAP210 results in compaction of Golgi structures in the peri-nuclear region, fragmentation of the Golgi ribbon and cisternal dilation (Bird et al., 2018; Sato et al., 2015; Smits et al., 2010; Wehrle et al., 2019; Yamaguchi et al., 2021). We also note the concurrent unstacking of cisternae and build-up of tubulovesicular membranes in the peri-Golgi region. Altogether, this is indicative of a severe, general disruption to Golgi membrane dynamics. In 2014, Wong *et al* demonstrated that GMAP210 tethers GalNAcT2 containing vesicles and supports the correct localisation of the golgins giantin and GCC88 (Wong and Munro, 2014). Its loss may therefore impact enzyme sorting and transport directly, whilst indirectly triggering a cascade of problems in membrane trafficking by causing the mis-localisation of other Golgi organising proteins.

Loss of Golgin-160 did not seem to affect Golgi stacking or cisternal flattening, however there was a clear build-up of transport vesicles. Unfortunately, we were unable to confirm whether these were COPI vesicles at the light level as individual vesicles could not be distinguished in the peri-Golgi region. Regardless, the large number of vesicles in the peri-Golgi region in KO cells is consistent with a loss of vesicle tethering function, which may explain the large number of cargoes negatively impacted by Golgin-160 loss. A second feature of Golgi organisation in Golgin-160 KO cells was fragmentation of the Golgi ribbon. It has been reported that Golgin-160 recruits dynein to Golgi membranes (Yadav et al., 2012). Microtubules are required to support lateral tethering of cisternae, and thus reduced motor and microtubule recruitment in the absence of Golgin-160 may underly this phenotype. Note, we did not observe the Golgi positioning or anterograde transport defects reported previously in another system (Yadav et al., 2012).

In humans, severe and hypomorphic mutations in the Trip11 gene encoding GMAP210 cause achondrogenesis type 1A (ACG1A) and odontochondrodysplasia (OCDC) respectively, (Costantini et al., 2021; Del Pino et al., 2021; Medina et al., 2020; Qian et al., 2021; Upadhyai et al., 2021; Wehrle et al., 2019). These diseases are characterised by skeletal abnormalities such as shortened ribs and cranial-facial malformations. Study of *Trip11* KO mouse models has ascertained that a primary driver

419 of pathology is defective ECM secretion during skeletal development (Bird et al., 2018; Follit et al.,
420 2008; Smits et al., 2010; Yamaguchi et al., 2021). Here we report a comparable attenuation of ECM
421 secretion in our GMAP210 KO epithelial lines, with many of our phenotypes recapitulating those of *in*
422 *vivo* and patient studies, including impaired collagen fibrillogenesis (Yamaguchi et al., 2021) and
423 diminished production of highly glycanated proteoglycans (Wehrle et al., 2019). Interesting, skeletal
424 dysplasia has not been reported in existing studies of *Golga3/Golgin-160* mutant mice (Banu et al.,
425 2002; Bentson et al., 2013; Matsukuma et al., 1999), which seems incongruous with the similarities
426 seen here between GMAP210 and Golgin-160 KO ECM defects. Compensatory mechanisms often
427 mask severe phenotypes in golgin mutant animal models, which may explain this discrepancy
428 (Bergen et al., 2017). Whether more subtle *in vivo* phenotypes, such as altered bone mass density
429 will be found with more extensive investigation remains to be determined.
430
431 Golgin-160 negatively impacted the secretion of a greater number of ECM components than
432 GMAP210, including several laminins and metalloproteases. This implies it has a greater impact on
433 transport. Consistent with this, Golgin-160 has been shown to bind to the Golgi-associated PDZ
434 domain containing protein PIST/GOPC (Hicks and Machamer, 2005), which supports transport of
435 cargoes to the plasma membrane. More specifically, the anterograde trafficking of the membrane-
436 bound GLUT4 transporter (Williams et al., 2006) and β4 adrenergic receptor (Hicks et al., 2006) has
437 been shown to require Golgin-160. Our results expand the list of golgin-160 dependent cargoes in
438 the context of soluble protein secretion and show that extracellular matrix components are
439 particularly affected.

440 Overall, whilst Golgin-160 KO had a primarily negative impact on general secretion, more than half of
441 the cargoes impacted by GMAP210 loss showed increased secretion in KO cells compared to WT.
442 Interestingly this was not the case for ECM proteins, which were almost always negatively impacted.
443 One family of proteins specifically impacted by GMAP210 KO were the lysosomal enzymes
444 cathepsins, four of which were aberrantly secreted by KO cells. This raises the possibility that the
445 increased abundance of certain proteins in GMAP210 KO culture medium may stem from sorting
446 defects. Interestingly, secreted cathepsins have been implicated in ECM degradation (Vidak et al.,
447 2019; Vizovisek et al., 2019). Of note, two of those identified here (cathepsins B + K) have been
448 shown to cleave targets such as SPARC (Podgorski et al., 2009), collagen type IV (Guinec et al., 1993),
449 and fibronectin (Guinec et al., 1993), which were all reduced in abundance in the same KO media.
450 Whether secreted cathepsins are contributing to the ECM phenotypes observed here therefore
451 remains an intriguing open question, especially considering their potential as drug targets if found to
452 contribute to disease pathology (Jangra et al., 2024).
453
454 Proteoglycans appear particularly susceptible to the loss of both GMAP210 and Golgin-160, with KO
455 affecting both gene expression and glycanation of biglycan. The biosynthetic pathway for GAG chains
456 serves as an excellent example of the importance of Golgi organisation (Hellicar et al., 2022; Ricard-
457 Blum et al., 2024). Chains are built by enzymes organised sequentially across the Golgi stack and
458 competition between enzymes determines which types of GAG chains are built. Consequently, chain
459 chemistry is determined by relative enzyme abundance, enzyme distribution, and trafficking speeds,
460 making it particularly sensitive to a variety of Golgi perturbations (Adusumalli et al., 2021; Ahat et al.,
461 2022; Chang et al., 2013). In our case, a common structural feature in both GMAP210 and Golgin-160
462 KO lines is Golgi fragmentation. Previously, this has been shown to disrupt the balance of GAG chain

species (Ahat et al., 2022; Harada et al., 2024) and reduce overall GAG sulphation (Ahat et al., 2022). We also find that nocodazole-induced Golgi fragmentation in RPE1 cells impairs biglycan GAG modification. Interestingly, nocodazole treatment of our mutant lines exacerbated glycan defects, suggesting that Golgi fragmentation is not fully pervasive. It is therefore worth considering the role of other golgin-specific changes to Golgi morphology.

The most prominent feature of Golgin-160 KO cells was the accumulation of transport vesicles. Loss of the COPI-binding COG complex has previously been shown to interfere with GAG chain length (Adusumalli et al., 2021), presumably due to impaired enzyme recycling. Thus, disruption to vesicular transport may contribute to glycan assembly defects in Golgin-160 KO cells. Meanwhile, a striking feature of GMAP210 KO cells was cisternal dilation, a feature also seen following the treatment of cells with actin destabilising drugs (Lazaro-Dieguez et al., 2006). One such drug, cytochalasin B, also inhibits proteoglycan synthesis without impacting secretion (Lohmander et al., 1979). Thus, cisternal dilation may contribute to glycan under-modification in the KO cells, perhaps by impacting the frequency with which membrane-bound enzymes interact with soluble luminal cargo and so reducing the efficiency of modification. Overall, it seems likely that the combined effect of different perturbations to Golgi homeostasis in each mutant cell line contribute to impaired glycanation.

In conclusion, we propose that golgins have distinct, non-redundant functions but work collectively to create the correct physical and biochemical space to support efficient ECM protein secretion and modification.

Figure Legends

Figure 1 – Extracellular matrix organisation is altered in golgin mutant cultures

A, C. Confocal maximum projection images of unpermeabilised WT, GMAP210 KO (A) and Golgin-160 KO (C) RPE1 cell cultures immunolabelled for extracellular collagen type I (green), fibronectin-1 (magenta) and nuclei (DAPI, blue). Scale bars 10 µm. **B, D.** Quantification of fibril characteristics measured from images represented in (A,C). Individual dots represent mean of each biological replicate (n=4) and bars represent median of all experiments. **E.** Decellularised ECM from WT, GMAP210 KO and Golgin-160 KO cell cultures imaged by HS-AFM. Images are representative 10 x 10 raster scans from biological replicates (n=3). Scale bars 10 µm. **F.** Quantification of fibril characteristics measured from images represented in (E). Individual dots are measurements from each tile in the raster scan, with each biological replicate colour coded (n=4). Bars represent median of all experiments. **B ,D, F.** Data were subjected to a Shapiro Wilk test for normality and then a nested one way analysis of variance (ANOVA) with Dunnet's test for multiple comparisons to generate p values.

Figure 2 – Collagen deposition in the matrix is impaired in golgin mutant cells

A. Immunoblot for Col1a1 and total protein stain after SDS-PAGE of medium (M) and lysate (L) samples taken from wildtype and golgin mutant cultures. **B.** Immunoblot for Col1a1 and total protein stain after SDS-PAGE of the cell derived matrix extracted from wildtype and golgin mutant cultures. **C.** Quantification of Col1a1 intensity normalised against total cellular protein for **i.** lysates samples as

503 represented in A and **ii.** matrix samples as represented in B. Dots show individual experiment result
504 (n=3), bars show mean and standard deviation. Data were subjected to a Shapiro Wilk test for
505 normality and then a nested one-way ANOVA with Dunnet's test for multiple comparisons to
506 generate p values.

507

508 **Figure 3 – Extracellular matrix composition is altered in golgin KO cells**

509 **A-B.** Volcano plots showing log-fold change in cell-derived matrix protein abundance from GMAP210
510 KO (A) or Golgin-160 KO (B) cells compared to WT. Red-labelled points represent proteins with
511 significantly changing abundance, with Benjamini-Hochberg false discover rate (FDR) corrected *p*-
512 values < 0.05, n=3. Only proteins categorised as 'matrisome' are represented on these plots (Naba
513 2011). Results for two different clones per gene are shown (i,ii). **C.** Heat map comparing protein
514 abundance changes between the two different golgin KOs after pooling both clones. Red and blue
515 indicate increased and decreased abundance respectively. Colour intensity is determined by average
516 log-fold change across mutants compared to WT.

517

518 **Figure 4** – **Golgi organisation is altered upon loss of GMAP210 or Golgin-160.**

519 **A, C.** Maximum projection confocal images of WT and GMAP210 KO (A) and Golgin-160 KO (C) RPE1
520 cells immunolabelled for cis-Golgi (GM130, magenta), cis-medial-Golgi (Giantin, green) and trans
521 Golgi network (TGN46, blue) markers. Nuclei labelled with DAPI (greyscale). Scale bar 10 µm. Inset
522 scale bar 1 µm. **B, D.** Quantification of total giantin and TGN46 area and fragment number per cell
523 from images represented in (A,C). Individual dots represent one cell and are coloured by replicate
524 (n=3). Bars show the median from each replicate experiment. Statistical analysis performed using
525 Shapiro-Wilk normality test and Kruskall-Wallis significance test. **E-G.** Tomographic reconstructions of
526 Golgi structures in WT (E), GMAP210 KO (F), and Golgin-160 KO (G) cells. Segmented membranes are
527 labelled as cisternae (blue/purple), dilated structures (red), tubulovesicular structures (yellow), and
528 vesicles (green). **Eii, Fii-iii, Gii-iii** Single slice images with segmentation. **Fii-iii** Open arrows point to
529 invaginations within spherical regions of tubulovesicular structures. **Gii-iii** Double headed arrows
530 indicate top to bottom fenestrations in cisternae, closed headed arrows indicate budding structures
531 at the nuclear envelope, pink arrow shows frustrated budding/fusion intermediate. **Ei, iii-iv, Fi, iv, v,**
532 **Gi, iv, v.** 3D rendering of segmentation. **E-Gi.** Scale bar 1 µm.

533

534 **Figure 5 – General secretion is differentially impacted by loss of GMAP210 or Golgin-160**

535 **A.** Volcano plots showing log-fold change in protein abundance in the media from KO versus WT
536 cultures plotted against significance across three independent replicate experiments. The results
537 from the two golgin KO clonal cell lines were pooled to increase power. Lines and dot colours on the
538 graph are for p<0.06 and >1 or <-1 LogFC. Triangular points show hits which pass an FDR corrected
539 p<0.05. Structural ECM proteins (i), ECM regulators (ii) and other proteins of interest (iii) have been
540 highlighted. Proteins significantly changed in the same way in both KO cultures are labelled in dark
541 blue whilst proteins impacted in a golgin specific way are labelled in purple. The proteoglycan family
542 is indicated by green text. **B-F.** RT-PCR analysis of gene expression of (B) BGN, (C) ARHGDIB, (D)

543 FAM20C, (E) PLOD1, and (F) THBS1. Expression levels normalised to expression of housekeeping gene
544 YWHAZ. Individual data points represent biological replicate experiments (n=3-4). Bars show mean
545 and standard deviation.

546

547 **Figure 6 – Biglycan can traffic efficiently in golgin KO cells**

548 **A-D.** Biglycan RUSH assay in WT (A), GMAP210 KO (B) and Golgin-160 KO (C) cells stably expressing
549 BGN-SBP-mSc (magenta) and transiently transfected with an ER hook (not visible) and Mannosidase
550 II-BFP (green) prior to experiment. **A-C.** Single plane confocal images taken from time-lapse movies of
551 biglycan transport after release from the ER by biotin addition at T 00:00. Time post biotin addition is
552 indicated in top left corner as mm:ss. **Ai, Bi, Ci.** White arrows highlight the emergence of post-Golgi
553 carriers. Scale bar 10 µm. **Aii, Bii, Ciii.** Crop showing incidence of ER-Golgi transport of biglycan as
554 highlighted by arrow. Scale bar 1 µm. **Aiii, Biii, Ciii.** Crop showing incidence of post-Golgi transport of
555 biglycan with carrier highlighted by arrow. Scale bar is 1 µm. **D.** Quantification of ER-Golgi transport,
556 measured as time between biotin addition and the appearance of biglycan signal adjacent to
557 Mannosidase II-BFP label. **E.** Quantification of Golgi transit time, measured as the time between
558 biglycan enrichment adjacent to mannosidase II-BFP signal and the emergence of a visible post-Golgi
559 carrier. **D-E.** All quantification performed on live movies as represented in A-C. Individual data points
560 represent individual cells imaged across six independent experiments, bars show mean and standard
561 deviation. **D.** Data were subjected to a Shapiro Wilk test for normality (failed) and then a nested one
562 way ANOVA with Kruskall-Wallis test. **E.** Data were subjected to a Shapiro Wilk test for normality
563 (passed) and then a nested one way ANOVA with Dunnet's test for multiple comparisons to generate
564 p values.

565

566 **Figure 7 – Biglycan is under-modified in golgin KO cells**

567 **A.** Western blots of media (M) and lysate (L) samples taken from WT, GMAP210 KO and Golgin-160
568 KO cells stably expressing BGN-SBP-mSc, probed with anti-RFP and anti-biglycan antibodies. **B.**
569 Quantification of the ratio between extracellular (M) and intracellular (L) biglycan in WT and KO
570 cultures, as determined by densitometry of the blots shown in (A). **C.** Quantification of the ratio
571 between 250kDa and 150kDa BGN bands present in the blots represented in (A). **B-C.** Dots represent
572 measurements from independent experiments, bars show mean and SD. Data were subjected to a
573 Shapiro Wilk test for normality (passed) and then a nested one way ANOVA with Dunnet's test for
574 multiple comparisons to generate p values. **D-E.** Western blots of medium and lysate samples from
575 WT and KO lines stably expressing BGN-SBP-mSc. Collected samples were treated with PNGase F (D)
576 or chondriotinase ABC (E) prior to SDS-PAGE. Blots probed with antibodies targeting the mSc tag. **D**.
577 Arrows depict undigested (top) and PNGaseF digested (bottom) core protein. **F.** Western blots of
578 medium and lysate samples from WT and KO lines stably expressing BGN-SBP-mSc. Media were
579 collected 5 hours after the addition of DMSO (control) or nocodazole to cultures. Immunoblot for
580 mSc tag (RFP).

581

582 **Supplemental Table 1 – GO term analysis of golgin Secretome data**

583 Proteins that showed significantly altered abundance in KO cell derived media compared to WT
584 conditioned media (p value < 0.01) were entered into the DAVID knowledgebase
585 (https://david.ncifcrf.gov/tools.jsp) and analysed against the Biological pathways GO-BP-DIRECT list
586 for Gene Ontology term enrichment. The 15 GO terms showing the most significant enrichment, as
587 determined by p-value, are presented here.

588

589 **Supplementary Figure 1 – Generation of CRISPR-Cas9 mutant lines**

590 **A.** CRISPR design and resulting mutations in chosen knockout clones. Top lines show gene sequence
591 in wildtype (WT) and mutant (KO) clones with encoded amino acid sequence underneath. Purple
592 lines indicate gRNA target sequence, scissors point to predicted Cas9 cut site, red letters in KO
593 sequences indicate mutagenic base pair insertions, purple letters in WT sequence indicate base pairs
594 deleted in the mutant lines. Green amino acids are mutagenic changes arising after frameshift in KO
595 lines and * denotes a premature stop codon. **B.** Maximum projection widefield images of WT and
596 GMAP210 KO lines immunolabelled as indicated. GMAP210 antibodies were raised against amino
597 acids 14-148 (N-term GMAP210), 159-365 (GMAP210), and 1760-1855 (C-term GMAP210). **C.**
598 Western blots of WT and GMAP210 KO cells probed with an antibody targeting amino acids 14-148
599 or GMAP210 (central well is an unsuccessful clone - X). **D.** Maximum projection widefield images of
600 WT and Golgin-160 KO clones labelled with GM130 (green, *cis*-Golgi) and Golgin-160 (magenta). **D.**
601 Western blot analysis of WT and Golgin-160 KO cell lysates probed with Golgin-160 antibodies and
602 tubulin and GAPDH as loading controls. **D, E.** Golgin-160 N-terminal and C-terminal antibodies raised
603 against amino acids 1-350 and 1436-1498 respectively.

604

605 **Supplemental Figure 2 – Matrisome analysis in mutant cells**

606 **A**. Principal component analysis of the mass spectrometry experiment shown in Figure 3. **B, C.** The
607 Col4a2 sequence was split into its structural features, abundances of relevant peptides were
608 averaged within each feature and plotted for each mutant. Total Col4a2 abundance was normalised
609 across conditions to investigate peptide level variation. N=3. **D.** Western blots of media (M) and
610 lysate (L) fractions from WT and Golgin-160 KO cell cultures stably expressing pro-SBP-GFP-COL1A1.
611 Blots probed with the LF39 antibody targeting the N-terminal propeptide domain of procollagen type
612 I and GAPDH as a housekeeping protein.

613

614 **Supplementary Figure 3 – Early secretory pathway organisation in golgin mutants**

615 **A-B.** Confocal maximum projection images of WT and golgin KO cell lines stained for cis/medial Golgi
616 membranes (giantin, magenta) markers and either ERGIC (ERGIC53, green) (A) or COP1 (βCOP, green)
617 structures (B). Scale bars 10 µM.

618

619 **Supplemental Figure 4 – Secretome analysis in mutant cells**

620 **A.** Log2 sum of raw peptide abundance in each proteomics replicate from the secretome analysis
621 shown in Figure 5. **B.** Principal component analysis of the secretome data sets represented in Figure

622 5. **C.** Heat map comparing protein abundance changes between the two different golgin KOs in the
623 secretome experiment. Red and blue indicate increased and decreased abundance respectively,
624 intensity of colour is determined by average log-fold change across mutants compared to WT.

625

626 **Supplementary Figure 5 – BGN-SBP-mSc localisation in mutant cells**

627 **A.** Widefield maximum projections of cells stable expressing BGN-SBP-mSc (blue) and
628 immunolabelled for the ERGIC (ERGIC53, green), cis/medial Golgi (giantin, magenta) and TGN
629 (TGN46, greyscale). Scale bar in main image 10 µm and insert 1 µm.

630

631 **Supplemental Movie 1 – Golgi reconstruction and segmentation in WT cell**

632 Electron tomographic reconstruction of a 250 nm section through a WT cell showing an organised
633 interconnected Golgi ribbon. Segmentation of a section of this ribbon shows cisternal membranes
634 (labelled in blue/purple), dilated structures at the TGN (red), tubulovesicular structures (yellow), and
635 vesicles (green). Movie shows slices running top-bottom-top through the section, then top to bottom
636 adding the segmentation, followed by a zoom and rotational views of the 3D segmented structures.
637 Movie runs at 40 frames per second.

638

639 **Supplemental Movie 2 – Golgi reconstruction and segmentation in GMAP210 KO2 cell**

640 Electron tomographic reconstruction of a 250 nm section through a GMAP210 KO2 cell showing
641 scattered and dilated Golgi structures. Segmentation of two closely apposed Golgi stacks shows
642 cisternal membranes (labelled in blue/purple), dilated structures (red), tubulovesicular structures
643 (yellow), and vesicles (green). Movie shows slices running top-bottom-top through the section, then
644 top to bottom adding the segmentation, followed by a zoom and rotational views of the 3D
645 segmented structures. Movie runs at 40 frames per second.

646

647 **Supplemental Movie 3 – Golgi reconstruction and segmentation in Golgin-160 KO2 cell**

648 Electron tomographic reconstruction of a 250 nm section through a Golgin-160 KO2 cell showing a
649 fragmented Golgi, with stacks surrounded by vesicles. Segmentation of one stack shows cisternal
650 membranes (labelled in blue/purple), dilated structures at the TGN (red), tubulovesicular structures
651 (yellow), and vesicles (green). Movie shows slices running top-bottom-top through the section, then
652 top to bottom adding the segmentation, then a zoom and rotational views of the 3D segmented
653 structures. Movie runs at 40 frames per second.

654

655 **Supplemental Movie 4 – Biglycan RUSH in WT cell**

656 Spinning disc confocal timelapse movie of a biglycan RUSH assay in a WT cell. Cells are stably
657 expressing BGN-SBP-mSc (magenta) and transiently expressing KDEL-streptavidin (unlabelled) and

658 Mannosidase-II-BFP (green). Movie begins 15 minutes after biotin addition (time after biotin
659 indicated in top left (mm:ss). One frame taken every 500 ms. Scale bar 10 µm.

660

661 **Supplemental Movie 5 – Biglycan RUSH in GMAP210 KO2 cell**

662 Spinning disc confocal timelapse movie of a biglycan RUSH assay in a GMAP210 KO2 cell. Cells are
663 stably expressing BGN-SBP-mSc (magenta) and transiently expressing KDEL-streptavidin (unlabelled)
664 and Mannosidase-II-BFP (green). Movie begins 15 minutes after biotin addition (time after biotin
665 indicated in top left (mm:ss). One frame taken every 500 ms. Scale bar 10 µm.

666

667 **Supplemental Movie 6 – Biglycan RUSH in Golgin-160 KO2 cell**

668 Spinning disc confocal timelapse movie of a biglycan RUSH assay in a Golgin-160 KO2 cell. Cells are
669 stably expressing BGN-SBP-mSc (magenta) and transiently expressing KDEL-streptavidin (unlabelled)
670 and Mannosidase-II-BFP (green). Movie begins 10 minutes after biotin addition (time after biotin
671 indicated in top left (mm:ss). One frame taken every 500 ms. Scale bar 10 µm.

672

673 **Methods**

674 *Cell culture*

675 Telomerase immortalised human retinal pigment epithelial cells (hTERT-RPE1) were purchased from
676 the American Type Culture Collection (ATCC) and grown in DMEM-F12-HAM (Life technologies
677 #11320-033) supplemented with 10% decomplemented fetal calf serum (FCS, Gibco A5256701),
678 passaging 1:10 every 3-4 days. HEK293T cells used for making lentivirus were grown in DMEM
679 (D5796) supplemented with 10% FCS. Transient transfections of RPE1 cells were performed using
680 Lipofectamine 2000 (Invitrogen catalog #11668027) and 2 µg DNA per 35 mm dish according to the
681 manufacturer's instructions. Stable cell lines were generated using Lenti-X™ Packaging Single Shots
682 kit (Takara, #631275) according to kit instructions and as described in the next section.

683 *Generating knockout cell lines*

684 *Transfection with RNPs:* To generate GMAP210 KO lines the IDT ALT-R™ CRISPR system was used
685 according to the manufacturer's protocols. Two crRNAs with sequences ATCCTGGAGTGCAATCTGTC
686 (designed by IDT and targeting exon 4) and TATTTGGTCGGATCGCCCGG (designed by Benchling
687 targeting exon 1) were ordered from IDT. To duplex the gRNAs, 1 µl of 1 nmol/µl Alt-R™ CRISPR-Cas9
688 crRNA and 1 µl of 1 nmol/µl Alt-R™ CRISPR-Cas9 tracrRNA (IDT #1072533) were mixed with 98 µl
689 duplex buffer (IDT #1072570) and heated to 95°C for 5 minutes before cooling on the bench. Alt-R™
690 S.p. Cas9 Nuclease V3 (IDT #10010588 LOT 000088243) was diluted to 1 µM in Cas9 working buffer
691 (20 nM HEPES, 150 nM KCl pH 7.5). To make the RNP, 1.5 µl duplexed gRNA + 1.5 µl 1 µM Cas9 + 0.6
692 µl Cas9 PLUS reagent (Invitrogen™ Lipofectamine™ CRISPRMAX™ #CMAX00001) + 21.4 µl optiMEM
693 were mixed per transfection. RNP mixes were left for 5 minutes at room temperature then 25 µl RNP
694 mix + 1.2 µl CRISPRMAX (Invitrogen™ Lipofectamine™ CRISPRMAX™ #CMAX00001) + 23.8 µl of
695 optiMEM (Gibco #31985-070) were added to a well of a 96 well plate. This was left to incubate for 20
696 minutes at room temperature. Meanwhile RPE1 cells were trypsinised, counted, centrifuged at 1000

697 xg for 3 minutes and then resuspended at a concentration of 20000 cells per 100 µl. After the 20-
698 minute transfection incubation, 100 µl cell suspension (20000 cells) was added to the wells and
699 plates put at 37°C 5% CO2. Cells were then expanded, and successful gene knockout was determined
700 by immunofluorescence staining of transfected cells.

701 *Transfection with lenti-CRISPR:* Golgin-160 KO lines were generated using lentiCRISPRv2 constructs.
702 To make the construct, two single stranded oligos targeting exon 20 of the GOLGA3 gene (transcript
703 GOLGA3-101 on ensemble) plus vector overhangs were ordered from IDT. Sequences: F1: 5'
704 CACCGCTGGACTTGACGGAGCAGCA 3' R1: 5' AAACTGCTGCTCCGTCAAGTCCAGC 3' (red is gene
705 targeting). Oligos were annealed in T4 ligation buffer (NEB #B0202A) with T4 PNK (NEB M0201S) for
706 30 minutes at 37°C followed by a 5-minute incubation at 95°C and cooling by ramping down to 25°C
707 at 5°C/minute. Annealed oligos were ligated into the lentiCRISPRv2 vector (Addgene Plasmid
708 #52961) overnight using T4 ligation buffer (NEB #B0202A) and T4 ligase (NEB #M0202S). Ligations
709 were transformed into One Shot™ Stbl3™ Chemically Competent *E. coli* (Invitrogen™ #C737303)
710 according to the manufacturer's instructions and bacterial cultures grown on ampicillin
711 supplemented agar plates (BD #214530). Successful ligation was determined by extracting constructs
712 with a QIAprep spin mini-prep kit (QIAGEN #27106) from bacterial colonies, followed by sequencing
713 (MWG Eurofin). The plasmid was then transfected into HEK293T cells using the Lenti-X™ Packaging
714 Single Shots kit (Takara Bio # 631278) according to kit instructions. After 48 hours, virus was
715 harvested and 8 µg/ml polybrene (Santa Cruz Technology sc-134220) added to a 1 ml aliquot. Media
716 was aspirated from a 6 cm dish of RPE1 cells and the virus aliquot added to cells for incubation for 1
717 hour at 37°C. DMEM-F12-HAM supplemented with 8 µg/ml polybrene was then added to cells and
718 cultures were incubated for 48 hours at 37°C. Transfected cells were selected at the next passage by
719 supplementing media with 10 µg/ml puromycin dihydrochloride (Santa-cruz technologies sc-
720 1080701). Successful gene editing was determined by immunofluorescence staining of transfected
721 cells.

722 *Making clones:* To identify gene edited cells, CRISPR/Cas9 transfected cell lines were single cell
723 sorted into a 96 well dish. Clones were expanded and KO confirmed by immunofluorescence and
724 western blot. DNA was extracted from confirmed KO clones using a PureLink genomic DNA mini kit
725 (Invitrogen #K1820-02) and the CRISPR target region was amplified by PCR using Q5® Hot Start High-
726 fidelity 2x master mix (NEB #M0493L) according to manufacturer's instructions and touch down PCR
727 programme: 1) 95°C for 3 minutes, 2) melt at 95°C for 25 seconds, 3) anneal at 72°C for 25 seconds,
728 4) extension at 72°C for 45 seconds, 5) repeat steps 2-4 reducing the annealing temperature by 0.5°C
729 per cycle x 20 cycles, 6) melt at 95°C for 25 seconds, 7) anneal at 72°C for 25 seconds, 8) extension at
730 72°C for 45 seconds 9) repeat steps 6-8 x25 10) 72°C 5 minutes 11) 4°C hold.

731 Golgin-160/GOLGA3 genotyping primers: Fwd 5'TGGGAGGTGGATCAGAAAGA3' Rev
732 5'ACCCTCCCATTTGCTGTAGT3'. GMAP210/TRIP11 genotyping primers for exon 4: Fwd 5'
733 GTTGATAGAGGACCATCATTGGA 3' Rev 5' TACACCAGCTCCTGAAGGTA 3'. GMAP210/TRIP11 primers
734 for exon 1: Fwd 5'TTCGTGGGAATGAGCAGAAG3' Rev 5' CAAGAGGAGGTGTGTGAAGAAA3'.

735 PCR products were purified using Qiaquick PCR purification kit (QIAGEN #28104) and A-tailed by
736 mixing 3 µl PCR product + 1 µl 10x Thermopol buffer (NEB M0267S) + 0.2 µl ATP + 1 µl Taq
737 polymerase and incubating the reaction at 70°C for 30 minutes. This reaction was then ligated into
738 pGEM t-easy vector with T4 ligase and T4 ligation buffer (Promega #A1360) so that individual alleles

739 could be sequenced. Sequencing was performed by MWG Eurofins using their stock T7 forward
740 primer.

741 *Cloning and constructs*

742 To make BGN-SBP-mSc, two gene blocks were designed using Hifi NEBuilder to encode the required
743 tagged biglycan protein plus accompanying flanking sequences for sequential assembly into the
744 pLVXNeo vector (Takara Bio #632181) using the NEB HiFi assembly system. The tagged biglycan
745 coding region consisted of the biglycan mRNA sequence (transcript ID: ENST00000331595.9, CCDS:
746 CCDS14721) followed by linker GSAGSAAGSGEF (Waldo et al., 1999), the streptavidin binding
747 protein sequence, linker GGGGSGGGGS, and the mScarlet-i coding sequence. pLVXNeo was digested
748 with XhoI (NEB #R0146S) in NEB 3.1 10x buffer (NEB #B7203S) for 15 minutes at 37C and then BsmBI-
749 V2 (NEB #R0739S) was added for a second digest at 55°C for 20 minutes. Reactions were heated to
750 80°C for 20 minutes to inactivate enzymes. Gene block 1 was assembled into the digested vector
751 with the Hifi assembly mix (NEB #E2621), and then the plasmid was transformed into NEB 5-alpha
752 cells (C2987H), both according to manufacturer's instructions. Colonies were grown up in LB plus
753 ampicillin and plasmids were extracted using a QIAprep spin mini-prep kit (QIAGEN #27106).
754 Successful assembly of insert into vector was confirmed by test digest with BsrGI and BamHI and
755 sequencing. This intermediate vector was then digested with XhoI and assembled with the second
756 block and confirmed as before.

757 Design of StrKDEL-IRES-mannosidase II-mTagBFP2 is detailed in (McCaughey et al., 2021) and
758 available on Addgene (Plasmid #165460). Design of the pro-col1a1-SBP-GFP plasmid is detailed in
759 (McCaughey et al., 2019) and available on Addgene (Plasmid #110726).

760 *Preparation of the cell derived matrix*

761 To collect the cell derived matrix, cells were grown to confluence (either on coverslips or plastic) and
762 their media supplemented with 50 µg/ml L-ascorbic acid-2-phosphate (Sigma-Aldrich A8960) for a
763 further 7 days. Cells were then washed in PBS and the cell layer removed by incubation with pre-
764 warmed extraction buffer (20 mM NH_4OH (Sigma-Aldricth #221228) and 0.5% Triton X-100) for three
765 minutes at room temperature. The dish was then washed three times with dH_2O and incubated with
766 10 µg/ml DNase I (Roche) diluted in reaction buffer (10 mM Tris-HCl, pH 7.6, 2.5 mM MgCl2, and 0.5
767 mM CaCl2) for 30 min at 37°C. After a further 3 washes in water, the cell derived matrix was either
768 fixed for staining or AFM imaging, or collected in sample buffer for assay (see appropriate section).
769

770 *Primary Antibodies*

Target	Company	Catalogue #	Lot #	Immunogen	Dilution	Fix
Golgin-160 C-term	Abcam	ab96080	GR323647	Human GOLGA3 aa 1400 to C-terminus	IF 1:1000 WB 1:500	PFA/MeOH
Golgin-160 N-term	Proteintech	21193-1-AP	00014538	1-350 aa encoded by BC142658	IF 1:1000 WB 1:500	PFA/MeOH

GMAP210 C-term	Sigma prestige	HPA070684	R98121	MLDDVQKKLMSLANSSEGKVDKVLMRNLFIGHFHTPKNQRHEVLRLMGSILGVRREEMEQLFHDDQGSVTRWMTGWLGGGSKSVPNTPLRPNQQSV	IF 1:500	PFA/MeOH
GMAP210 N-term	Sigma prestige	HPA002570	A95744	QSLGQVGGSLASLTGQISNFTKDMLMEGTEEVEAELPDSRTKEIEAIHAILRSENERLKKLCTDLEEKHEASEIQIKQQSTSYRNQLQQKEVEISHLKARQIALQDQLLKLQSAAQSVPSGAGVPATTASSSFAY	IF 1:500	PFA/MeOH
GMAP210	Bd Bioscience	BD611712	47539	Full length protein	IF 1:1000	PFA/MeOH
TGN46	Bio-rad	AHP500	170720	Full length human protein	IF 1:1000	PFA/MeOH
Giantin	Covance	PRB-114C	Clone 19243. B23348	N-terminus, residues 1-469, of human giantin	IF 1:2000	PFA/MeOH
GM130	BD Bioscience	*BD610823, RRID:AB_398142*	3161628	Rat GM130 aa. 869-982	IF 1:1000	PFA/MeOH
Biglycan	Abcam	ab188508	Gr2a5102.3	Proprietary information	WB 1:500	-
RFP (mScarlet)	Chromotek	6G6-100	51020014AB	Full length protein	WB 1:1000	-
bCOP	Sigma	G6160	asceites	synthetic peptide D1 of β-COP (a.a. 701-715)	IF 1:200	MeOH
LMAN1/ERGIC53	Invitrogen	MA5-25345	WH3358331	Full length human protein	IF 1:1000	MeOH
Fibronectin	Sigma	F7387	Unknown	fibronectin from human plasma	IF 1:1000	-
Collagen type 1	Novus Biologicals	NB600-408, RRID:AB_10000511	38825	Collagen I from human and bovine placenta	IF 1:1000 WB 1:500	PFA
A-Tubulin	Sigma aldritch	T5168; RRID:AB_477579	Unknown	Sarkosyl-resistant filaments from *Strongylocentrotus purpuratus* (sea urchin) sperm axoneme	WB 1:2000	-

Immunofluorescence and fixed cell microscopy

773 For antibody labelling, cells grown on autoclaved coverslips (Menzel #1.5, Fisher Scientific) were fixed
774 with 4% PFA (Fisher-Scientific P/0840/53) for 10 minutes followed by permeabilisation for 10 minutes
775 with 0.1% Tx100 (Sigma-Aldritch #X100) at room temperature. For ER antibodies, cells were fixed
776 with MeOH (Sigma-Aldritch #32213) for 3 minutes at -20°C. Cells were then blocked with 3% BSA
777 (Sigma-Aldritch #A9647) for 30 minutes before incubation with primary antibody for 30 minutes,
778 three washes with PBS, and incubation with Alexa Fluor conjugated secondary antibody (Invitrogen).
779 After a further three washes, cells were labelled with DAPI (4,6-diamidino-2-phenylindole; Life
780 Technologies, D1306) for two minutes, washed in PBS, and mounted on glass slides in MOWIOL 4-88
781 (Calbiochem #475904). For immunolabelling of extracellular matrix, cells were PFA fixed and stained
782 without permeabilization. Collagen and fibronectin fibrillar features were analysed using the matrix
783 analysis Fiji macro TWOMBLI (Wershof et al., 2021).

784 Widefield images of fixed cells were taken using an Olympus IX70 microscope with 60x 1.42 NA oil-
785 immersion lens, Exfo 120 metal halide illumination with excitation, dichroic and emission filters
786 (Semrock, Rochester, NY), and a Photometrics Coolsnap HQ2 CCD, controlled by Volocity 5.4.1 (Perkin
787 Elmer). Chromatic shifts in images were registration corrected using TetraSpek fluorescent beads
788 (Thermo Fisher). Images were acquired as Δ0.2 µm *z*-stacks.

789 Confocal microscopy was performed using one of two systems. One, a Leica SP5II AOBS (Acousto-
790 Optical Beam Splitter) confocal laser scanning microscope equipped with 50mW 405nm laser, 150
791 mW Argon laser, 20mW solid state yellow laser, 20 mW Red He/Ne diode laser, photomultiplier tube
792 detectors and a 63x HCX PL APO CS oil objective. Or two, a Leica SP8 AOBS (Acousto-Optical Beam
793 Splitter) confocal laser scanning microscope equipped with 65 mW Argon laser, 20 mW DPSS yellow
794 laser, 10 mW Red He/Ne and 50 mW 405 nm diode laser, hybrid detectors, and a 63x HC PL APO CS2
795 oil objective. Images were acquired at 1024 × 1024 x-y resolution, averaging three line scans per
796 channel, using LAS X software. Image stacks were taken with Δz of 0.2 µm.

797 Golgi area and fragmentation were measured from confocal images using an image J macro with the
798 following procedures: Subtract background (rolling ball size 20), apply median filter (radius
799 determined individual experiments), apply threshold (set for each experiment), make binary, analyse
800 particles (size >0.1).

801 *Electron microscopy*

802 Cells were grown to confluence in 35mm dishes and then fixed *in situ* in 2.5% glutaraldehyde/0.1 M
803 cacodylate buffer for 20 minutes. Cells were then washed with 0.1 M cacodylate buffer for 10
804 minutes and fixed in 1% OsO4, 1.5% potassium ferro-cyanide, 0.1 M cacodylate buffer for 60
805 minutes. Cells were then washed with 0.1 M cacodylate buffer twice, and with water twice for 10
806 minutes each. To negative stain, cells were incubated with 3% uranyl acetate for 20 minutes and
807 washed again with water. Samples were then dehydrated by successive 10-minute incubations with
808 70%, 80%, 90%, 96% and 100% EtOH. After a second 100% EtOH incubation, all EtOH was removed
809 and approximately 1ml of a 50:50 mix of propylene oxide and epon was added to the dish. Samples
810 were placed on a rocker for two hours. This was exchanged with 100% epon before placing resin
811 stubs in the dish and baking the samples at 70°C for two days. Stubs were extracted from the dish
812 and trimmed. Ultrathin sections of 70 nm were cut using a diamond knife and a UC6 ultramicrotome
813 (Leica Microsystems) and incubated with 10 nm gold nanoparticles to act as fiducials (Sigma-Aldrich
814 #752584). Sections were imaged using a Tecnai20 LaB6 200k kV twin lens transmission electron

815 microscope (FEI) to collect a tilt series between -70° and +70° using a dedicated Fischione
816 tomography holder and FEI software. Tomograms were reconstructed using IMOD© software.
817 Alignment was computed using fiducial tracking and tomograms generated using 10 iterations with
818 SIRT-like filter reconstruction. Segmentation was performed using Amira 2019.3 software.

819

820 *AFM*

821 Cells were grown on coverslips and the cell derived matrix processed as above and then fixed in 4%
822 PFA (Fisher-Scientific P/0840/53) for 10 minutes at room temperature. Coverslips were rinsed with
823 deionised water to remove salt crystals visible in the HS-AFM images and mounted onto SEM stubs.
824 Excess water was blown off with compressed gas and samples were stored at room temperature
825 prior to HS-AFM imaging. Imaging was performed with a HS-AFM (Bristol Nanodynamics) and a
826 MSNL -10 cantilever chip (Bruker). One hundred images in 10 x 10 raster scans were collected in
827 three different areas of each coverslip. Imaging and analysis of the samples was performed blind.
828 Fibrillar features were analysed from the images of one raster scan from each biological replicate
829 (n=3) with the matrix analysis Fiji macro TWOMBLI (Wershof et al., 2021). Identical TWOMBLI
830 parameters were used for all samples. Periodicity was determined by extracting the peak profiles
831 along fibrillar structures using Gwyddion 2.60. The period was calculated using Excel and data
832 displayed/analysed with Graphpad Prism 10.0.2.
833

834 *Live imaging of RUSH assays*

835 For live imaging RUSH experiments, cells stably expressing BGN-SBP-mSc were grown to confluence
836 in 35 mm Mattek glass bottom imaging dishes (MatTek P35G-1.5-20C) and transiently transfected
837 with ManII-BFP_IRES_KDEL-streptavidin (McCaughey et al., 2021) 24 hours prior to imaging. To
838 image, growth media was replaced with 1 ml pre-warmed Fluorobrite DMEM (Thermo-Fisher
839 Scientific; A1896701) and dishes were mounted on an Olympus IXplore spinning disk system in a light
840 excluding environmental control chamber (PECON) at 37°C. At T0, 1 ml fluorobrite media containing
841 80 µM biotin was added to the dish (final concentration 40 µm) and imaging immediately started,
842 taking 120 frames every 10 seconds followed by 4800 frames every 500 ms. Data were acquired
843 using a 60x oil immersion lens with 1.5 numerical aperture, Hamamatsu Fusion BT sCMOS cameras,
844 diode lasers, TruFocus drift compensation, and Olympus CellSens imaging software. The frame at
845 which mScarlet signal could first be seen accumulating adjacent to the BFP signal was used to
846 measure transit to Golgi time. The frame in which a tubular carrier could first be seen emerging from
847 the BFP signal (that then continues to the periphery) was used to calculate Golgi transit time.

848 *Secretion assays*

849 To perform secretion assays, cells were seeded in 6 well dishes and grown to confluence before
850 aspirating their growth medium and replacing this with 1ml serum-free DMEM F12-HAM. After
851 overnight incubation at 37°C/5% CO2, cells were put on ice, the media was collected into eppendorfs
852 and the cell layer washed with ice cold PBS. Cells were then lysed in RIPA buffer (50 mM Tris-HCl, pH
853 7.5, 300 mM NaCl, 2% Triton X-100, 1% deoxycholate, 0.1% SDS, 1 mM EDTA) containing protease
854 inhibitors (Millipore #539137) on ice for 15 minutes on a rocker. Media samples were centrifuged at
855 2000 xg for 2 minutes at 4°C to remove dead cells and the supernatant collected. RIPA lysates were
856 scraped up into eppendorfs and centrifuged for 10 minutes at 13000 xg/4°C and the supernatant

857 collected. Media and lysates were then mixed with 4x Bolt™ LDS sample buffer (Invitrogen™
858 #B0007), boiled for 10 minutes at 70°C and run on SDS-PAGE gels as below.

859 For nocodazole secretion assays, cell media was replaced with 1ml serum-free DMEM F12-HAM
860 supplemented with 20 µM nocodazole or an equivalent volume of DMSO as vehicle control for 5
861 hours. Beyond this point cells were beginning to round and longer collections were not possible.
862 Media and lysates were then collected as normal.

863 For normal cell lysate collection and western blotting, cells were lysed in RIPA buffer and processed
864 as above. For cell-derived matrix samples, prewarmed sample buffer with reducing agent was added
865 to the dish after cell extraction (above), the dishes were scraped and the buffer collected and boiled
866 for 10 minutes at 70°C.

867 *Deglycosylation assays*

868 WT and KO cells stably expressing BGN-SBP-mSc were grown to confluence in a 150 mm dish and
869 media exchanged for serum free media 16 hours prior to experiment. Media was then collected into
870 falcon tubes on ice and spun at 1200 rpm for 2 minutes to pellet out cells. The supernatant was
871 collected, supplemented with a protease inhibitor cocktail (Millipore #539137) and BGN-SBP-mSc
872 extracted by RFP trap. To trap, a 60 µl aliquot of Chromotek RFP-trap® agarose beads (Chromotek
873 #rta) was washed 3x in a falcon tube with dilution buffer (10mM Tris/Hcl pH7.4, 50mM NaCl, 0.5mM
874 EDTA), centrifuging for 2 minutes at 2000 rpm at 4°C each time to pellet the beads for buffer
875 exchange. On the final wash, all buffer was removed and the media supernatant added to the beads.
876 Beads and sample were mixed on a rotator at 4°C for 2 hours. Tubes were spun at 2700 xg for 2
877 minutes at 4°C to pellet the beads and the media removed. Beads were then washed 3x as before in
878 dilution buffer supplemented with protease inhibitors. After the removal of the final wash, the beads
879 were purged.

880 *For digest with PNGase (kit, NEB P0704S)*, 10x glycoprotein denaturation buffer was diluted to 1x
881 with water and then 80 µl of this added to the bead pellet. Beads and buffer were transferred to an
882 Eppendorf tube and then heated at 100°C for 10 minutes. Samples were then put on ice for 10
883 seconds before centrifuging them at 2700 xg for 2 minutes. A 60 µl aliquot of the supernatant was
884 transferred to a new tube to act as an undigested control. The remaining 20 µl were transferred to a
885 new tube and contents were digested by adding 4 µl 2x Glycobuffer 2, 4 µl 10% NP40, 10 µl of water,
886 and 2 µl of PNGase F and incubating the mix at 37°C for one hour. Samples were cooled to room
887 temperature, mixed with 4x Bolt™ LDS sample buffer (Invitrogen™ #B0007) and analysed by SDS-
888 PAGE as below.

889 *For digest with Chondroitinase ABC (Merck Life Science Limited)*, bead pellets were resuspended in
890 200 µl dilution buffer (50 mM Tris HCl pH8, 60 mM sodium acetate, 0.02% BSA) and heated at 65°C
891 for 30 minutes to heat inactivate any residual proteases. Of this suspension, 100 µl was then taken
892 and 0.3U chondroitinase ABC added (digested sample). The remaining 100 µl was left untreated
893 (undigested). All samples were incubated at 37°C overnight. 4x Bolt™ LDS sample buffer (Invitrogen™
894 #B0007) was added, and samples boiled at 70°C ready for western blotting as below.

895 *Western blotting*

896 Samples were run in Bolt 4-12% bis-tris gels with MOPS running buffer for 40 minutes at 130 V. They
897 were then transferred to 0.2 µM nitrocellulose membranes and blocked with 5% milk-TBST. Primary

898 antibody incubations were run overnight at 4°C, then membranes were washed with TBS-0.05%
899 tween (Sigma-Aldrich) and incubated with HRP- (Jackson ImmunoResearch) or fluorophore-
900 conjugated (Invitrogen) secondary antibodies for 2 hours prior to imaging by enhanced
901 chemiluminescence (Promega ECL) and autoradiography films (GE Healthcare) or by fluorescence
902 imaging (LiCor Odyssey) respectively. For collagen blotting, samples were ran on NuPAGE 3-8% tris-
903 acetate gels at 120 V for 1 hour and transferred onto 0.45 µm PVDF membranes overnight at 12 V
904 and 4 °C. Membrane total protein staining was performed with a total protein stain kit (Licor).
905 Quantification of band intensity was performed with image J or Empiria Studio 3.0.

906 *Matrisome proteomics*

907 Cells were grown in 15 cm dishes for one week in the presence of 50 µg/ml L-ascorbic acid-2-
908 phosphate (Sigma-Aldrich A8960). Cells were then extracted and the cell derived matrix was
909 collected by adding 1 ml PBS to the plate and scraping for 30 seconds. Samples were transferred to
910 tubes and frozen at -20°C prior to processing.

911 Lysis buffer (10% sodium dodecyl sulfate (Sigma Aldrich) in 50 mM TEAB (Sigma-Aldrich)
912 supplemented with protease and phosphatase inhibitors) was added (1:1 v/v). Samples were
913 sonicated using a Covaris LE220+ sonicator using a 40 W lysis programme with 100 cycles per burst, a
914 duty factor of 40% and a peak incident power of 500 W. Next, 50 µg of protein was reduced and
915 alkylated using DTT (final concentration 5 mM) and IAA (final concentration 15 mM) respectively.
916 Samples were acidified with H_3PO_4 (1.2% final concentration), then 7 volumes of Binding buffer (90%
917 methanol, 10% distilled water; 100 mM TEAB) was added and the samples were loaded onto S-Trap
918 columns (ProtiFi) according to the manufacturer's protocol.

919 Column-bound proteins were washed in Binding buffer and then digested with 5 µg of 0.8 µg/µL
920 trypsin solution (Promega) diluted in Digestion buffer (50 mM TEAB at pH 8.5). Peptides were eluted
921 from the column in 65 µL Digestion buffer, 65 µl 0.1% formic acid (FA) in distilled water and finally
922 with 30 µL 0.1% FA, 30% acetonitrile (ACN, Sigma). Peptides were desalted using Oligo R3 resin beads
923 (Thermo Scientific), according to the manufacturer's protocol, in a 96-well, 0.2 µm polyvinylidene
924 fluoride (PVDF) filter plate (Corning). The immobilised peptides were washed twice with 0.1% FA
925 prior to 2 x 50 µl elutions in 0.1% FA with 30% ACN, and lyophilisation using a speed-vac (Heto
926 Cooling System).

927 Peptides were resuspended in 10 µL 0.1% FA in 5% ACN. Liquid chromatography (LC) separation was
928 performed on a Thermo RSLC system consisting of an NCP3200RS nano pump, WPS3000TPS
929 autosampler and TCC3000RS column oven configured with buffer A as 0.1% FA in water and buffer B
930 as 0.1% DA in ACN. The analytical column (Waters nanoEase M/Z Peptide CSH C18 Column, 130 Å,
931 1.7 µm, 75 µm x 250 mm) was kept at 35°C and at a flow rate of 300 nL/minute for 8 minutes. The
932 injection valve was set to load before a separation consisting of a 105 minute multistage gradient
933 ranging from 2 to 65% of buffer B. The LC system was coupled to a Thermo Exploris 480 mass
934 spectrometry system via a Thermo Nanospray Flex ion source. The nanospray voltage was set at 1900
935 V and the ion transfer tube temperature set to 275°C. Data was acquired in a data-dependent
936 manner using a fixed cycle time of 2 seconds, an expected peak width of 15 seconds and a default
937 charge state of +2. Full mass spectra were acquired in positive mode over a scan range of 300 to
938 1750 Th, with a resolution of 120000, a normalised automatic gain control (AGC) target of 300% and
939 a max fill time of 25 ms for a single microscan. Fragmentation data was obtained from signals with a

charge state of +2 or +3 with an intensity over 5000. They were then dynamically excluded from further analysis for a period of 15 seconds after a single acquisition within a 10 ppm window. Fragmentation spectra were acquired with a resolution of 15000, a normalised collision energy of 30%, an AGC target of 300%, a first mass of 110 Th, and a maximum fill time of 25 ms for a single microscan. All data was collected in profile mode.

Mass spectrometry data was analysed using MaxQuant (v1.6.14) using default parameters. All searches included the fixed modification for carbamidomethylation on cysteine residues resulting from IAA treatment. The variable modifications included in the search were oxidised methionine (monoisotopic mass change, +15.955 Da), hydroxyproline (15.995 Da), acetylation of the protein N-terminus (42.011 Da) and phosphorylation of threonine, serine and tyrosine (79.966 Da). A maximum of 2 missed cleavages per peptide was allowed. Peptides were searched against the UniProt database with a maximum false discovery rate of 1%. Proteins were required to have a minimum false discovery rate (FDR) of 1% and at least 2 unique peptides in order to be accepted, known contaminants were also removed. Missing values were assumed to be due to low abundance. Abundances were compared using MsqRob where label free quantification data was normalised using median peptide intensity (Goeminne et al., 2020). MsqRob was used using R (version 4.1.2). The remaining statistics were done using Prism (GraphPad Software, version 9.1.2).

Secretome proteomics

Cells were seeded into 6 well dishes and grown to confluence. Cells were rinsed once with serum free medium, taking care to aspirate as much media as possible each time. Exactly 1 ml serum free F12 HAM was then added to cells overnight. After 24 hours, cells were put on ice and 900 µl medium was removed from well and added to eppendorf on ice. Media were spun at 2000 rpm for 5 minutes and then 800 µl removed and put in a fresh tube on ice. To test protein concentration, 25 µl medium was used in a BSA assay prior to snap freezing and storage at -80 °C.

For TMT Labelling and High pH reversed-phase chromatography, an equal volume (95 µl) of each sample was digested with trypsin (1.25 µg trypsin; 37 °C, overnight), labelled with Tandem Mass Tag (TMTpro) sixteen plex reagents according to the manufacturer's protocol (Thermo Fisher Scientific, Loughborough, LE11 5RG, UK) and the labelled samples pooled. The pooled samples were desalted using a SepPak cartridge according to the manufacturer's instructions (Waters, Milford, Massachusetts, USA). Eluate from the SepPak cartridge was evaporated to dryness and resuspended in buffer A (20 mM ammonium hydroxide, pH 10) prior to fractionation by high pH reversed-phase chromatography using an Ultimate 3000 liquid chromatography system (Thermo Fisher Scientific). In brief, the sample was loaded onto an XBridge BEH C18 Column (130Å, 3.5 µm, 2.1 mm X 150 mm, Waters, UK) in buffer A and peptides eluted with an increasing gradient of buffer B (20 mM Ammonium Hydroxide in acetonitrile, pH 10) from 0-95% over 60 minutes. The resulting fractions (concatenated into 15 in total) were evaporated to dryness and resuspended in 1% formic acid prior to analysis by nano-LC MSMS using an Orbitrap Fusion Lumos mass spectrometer (Thermo Scientific).

High pH RP fractions were further fractionated using an Ultimate 3000 nano-LC system in line with an Orbitrap Fusion Lumos mass spectrometer (Thermo Scientific). In brief, peptides in 1% (vol/vol) formic acid were injected onto an Acclaim PepMap C18 nano-trap column (Thermo Scientific). After washing with 0.5% (vol/vol) acetonitrile 0.1% (vol/vol) formic acid peptides were resolved on a 250 mm × 75 µm Acclaim PepMap C18 reverse phase analytical column (Thermo Scientific) over a 150 min organic gradient, using 7 gradient segments (1-6% solvent B over 1min., 6-15% B over 58min., 15-32% B over 58min., 32-40% B over 5min., 40-90% B over 1min., held at 90% B for 6min and then

984 reduced to 1% B over 1min.) with a flow rate of 300 nl min^{-1}. Solvent A was 0.1% formic acid (FA) and
985 Solvent B was aqueous 80% acetonitrile in 0.1% formic acid. Peptides were ionized by nano-
986 electrospray ionization at 2.0 kV using a stainless-steel emitter with an internal diameter of 30 µm
987 (Thermo Scientific) and a capillary temperature of 300 °C.
988
989 All spectra were acquired using an Orbitrap Fusion Lumos mass spectrometer controlled by Xcalibur
990 3.0 software (Thermo Scientific) and operated in data-dependent acquisition mode using an SPS-MS3
991 workflow. FTMS1 spectra were collected at a resolution of 120 000, with an automatic gain control
992 (AGC) target of 200 000 and a max injection time of 50 ms. Precursors were filtered with an intensity
993 threshold of 5000, according to charge state (to include charge states 2-7) and with monoisotopic
994 peak determination set to Peptide. Previously interrogated precursors were excluded using a
995 dynamic window (60s +/-10ppm). The MS2 precursors were isolated with a quadrupole isolation
996 window of 0.7m/z. ITMS2 spectra were collected with an AGC target of 10 000, max injection time of
997 70ms and CID collision energy of 35%.
998
999 For FTMS3 analysis, the Orbitrap was operated at 50 000 resolution with an AGC target of 50 000 and
1000 a max injection time of 105 ms. Precursors were fragmented by high energy collision dissociation
1001 (HCD) at a normalised collision energy of 60% to ensure maximal TMT reporter ion yield.
1002 Synchronous Precursor Selection (SPS) was enabled to include up to 10 MS2 fragment ions in the
1003 FTMS3 scan.
1004
1005 The raw data files were processed and quantified using Proteome Discoverer software v2.1 (Thermo
1006 Scientific) and searched against the UniProt Human database (downloaded January 2023: 81579
1007 entries) and the Uniprot Bos taurus database (downloaded February 2023: 37505 entries) using the
1008 SEQUEST HT algorithm. Peptide precursor mass tolerance was set at 10ppm, and MS/MS tolerance
1009 was set at 0.6Da. Search criteria included oxidation of methionine (+15.995Da), acetylation of the
1010 protein N-terminus (+42.011Da) and Methionine loss plus acetylation of the protein N-terminus (-
1011 89.03Da) as variable modifications and carbamidomethylation of cysteine (+57.021Da) and the
1012 addition of the TMTpro mass tag (+304.207) to peptide N-termini and lysine as fixed modifications.
1013 Searches were performed with full tryptic digestion and a maximum of 2 missed cleavages were
1014 allowed. The reverse database search option was enabled and all data was filtered to satisfy false
1015 discovery rate (FDR) of 5%.

1016 As samples are from the media fraction of cultures, equal volumes of sample were analysed rather
1017 than equal quantities of protein, and raw abundances were used without normalisation. Statistical
1018 analysis was performed in R version 4.3.0. PCAs were calculated using the FactoMineR package,
1019 PCAs, Sum abundance, and volcano plots were plotted in ggplot2. A linear mixed effect model was
1020 fitted for each protein using the package lme4, with replicate number included as a random effect,
1021 and both clones included in a single variable for the KO condition to increase statistical power. P-
1022 values were then FDR adjusted using the Benjamini Hochberg method to account for multiple
1023 testing. Note, this was used as a gold-standard metric for individual proteins rather than a threshold
1024 for statistical analysis, as it is understood to be an overly stringent method for most proteomics
1025 experiments (Pascovici et al., 2016). Downstream analysis was performed using QIAGEN IPA (QIAGEN
1026 Inc., https://digitalinsights.qiagen.com/IPA), using $p<0.05$ as a cut-off and the unfiltered user data as
1027 the reference set (Kramer et al., 2014). GO term functional enrichment analysis was performed using
1028 the Database for Annotation, Visualization, and Integrated Discovery
1029 (DAVID; http://www.david.niaid.nih.gov).

1030

1031 *qPCR*

1032 Cells were grown to confluence in 35 mm dishes and then RNA was extracted using RNeasy® plus
1033 mini kit (QIAGEN #74136). Reverse transcription was performed using an Invitrogen Superscript III kit
1034 (Invitrogen™ #11752-050) following the manufacturer's instructions to generate cDNA. cDNA was
1035 diluted to 15 ng/µl and primers to 2 µM stocks. Reactions were set up using 3.75 ng/µl DNA, 500 nM
1036 forward and reverse primers, and 2x DyNAmo Flash Sybr green master mix (ThermoFisher Scientific
1037 #F415) in MicroAmp® optical 96-well reaction plates (Applied biosystems #N8010560). RT-PCR was
1038 then performed on a QuantStudio™ 3 real time PCR system using cycle: 1) 7 minutes @ 95°C, 2) 15
1039 seconds @ 95°C, 3) 45 seconds @ 60°C, 4) 40 cycles of steps 2-3. RT-PCR was followed by melting
1040 curve analysis at 60-98°C for quality control. PCR products were tested on a gel for size during primer
1041 validation. RT-PCR results were analysed with the QuantStudio™ real time PCR software.

1042 Primer sequences

Target	Forward primer	Reverse primer	Reference
YWHAZ	AGGCATGTCTGTGTCCTAATG	CCTCCATAACCCATTCTTCT	Designed with IDT
BGN	GGGTCTCCAGCACCTCTACGC	TGAACACTCCCTTGGGCACCT	Fang *et al* (Fang et al., 2019)
FAM20C	GGCGGCCGTGGACTCCTATC	TTGACCATCCTGCCGGCCAC	Designed with Primer3
PLOD1	TGGAGGCTTCATCGGTTATG	GATGTAGTTGCCCAGGTAGTT	Designed with Primer3
THSP1	TTGGAACCACACCAGAAGAC	GACACTCAGTGCAGCTATCAA	Designed with Primer3
ARHGDIB	ACCAATCACCATGGACCTTAC	AGGTGGTCTTGCTTGTCATC	Designed with Primer3

1043

1044 *Statistical analysis*

1045 All statistical analyses were performed with graphpad prism. Data were subjected to normality
1046 testing using the Shapiro-Wilk test. Data found to be normally distributed were analysed by t-test or
1047 one-way ANOVA and the mean and standard deviation shown. Non-normally distributed data were
1048 analysed with a Mann-Whiney test, or to compare multiple conditions Kruskall-Wallis test with
1049 Dunn's multiple comparisons, and the median and interquartile range presented. Statistical
1050 information is provided in each figure legend.

1051 **Acknowledgements**

1052 We would like to thank Andrew Herman and Poppy Miller of the UoB FACS facility with their help
1053 sorting CRISPR transfected cells, the UoB Wolfson facility, especially Judith Mantell and Dominic
1054 Alibhai, for training advice and facilities, David Knight and Stacey Harwood at the University of
1055 Manchester BioMS facility for running the matrisome samples, Prof Oliver Jenson and Dr Christopher
1056 Revell for conceptual discussions, Dr Anne George and Dr Harry Young for running pilot experiments,
1057 and Prof Stuart Haslam for advice. This work was funded by the UK Research and Innovation–
1058 Biotechnology and Biological Sciences Research Council BB/T001984/1.

1059 **CRediT Author contributions**

1060 Conceptualisation: D.J.S, N.L.S, M.L.; Methodology: N.L.S, G.T, A.H, K.H, P.A.L; Validation: N.L.S, G.T.;
1061 Formal analysis: N.L.S, P.A.L, A.H, G.T.; Investigation: N.L.S, G.T, A.H, E.P.S, K.H.; Writing draft: N.L.S,
1062 G.T, A.H, P.A.L; Writing review and editing: N.L.S, M.L; Visualisation: N.L.S., G.T, A.H, P.A.L;

Supervision: N.L.S, D.J.S, M.L., J.S; Project administration: N.L.S, D.J.S; Funding acquisition: D.J.S, M.L, N.L.S, J.S.

References

Adams, J.C. 2023. Passing the post: roles of posttranslational modifications in the form and function of extracellular matrix. *Am J Physiol Cell Physiol*. 324:C1179-C1197.

Adusumalli, R., H.C. Asheim, V. Lupashin, J.B. Blackburn, and K. Prydz. 2021. Proteoglycan synthesis in conserved oligomeric Golgi subunit deficient HEK293T cells is affected differently, depending on the lacking subunit. *Traffic*. 22:230-239.

Ahat, E., Y. Song, K. Xia, W. Reid, J. Li, S. Bui, F. Zhang, R.J. Linhardt, and Y. Wang. 2022. GRASP depletion-mediated Golgi fragmentation impairs glycosaminoglycan synthesis, sulfation, and secretion. *Cell Mol Life Sci*. 79:199.

Appenzeller-Herzog, C., and H.P. Hauri. 2006. The ER-Golgi intermediate compartment (ERGIC): in search of its identity and function. *J Cell Sci*. 119:2173-2183.

Arab, M., T. Chen, and M. Lowe. 2024. Mechanisms governing vesicle traffic at the Golgi apparatus. *Curr Opin Cell Biol*. 88:102365.

Arpino, V., M. Brock, and S.E. Gill. 2015. The role of TIMPs in regulation of extracellular matrix proteolysis. *Matrix Biol*. 44-46:247-254.

Banu, Y., M. Matsuda, M. Yoshihara, M. Kondo, S. Sutou, and S. Matsukuma. 2002. Golgi matrix protein gene, Golga3/Mea2, rearranged and re-expressed in pachytene spermatocytes restores spermatogenesis in the mouse. *Mol Reprod Dev*. 61:288-301.

Barr, F.A., and B. Short. 2003. Golgins in the structure and dynamics of the Golgi apparatus. *Curr Opin Cell Biol*. 15:405-413.

Bentson, L.F., V.A. Agbor, L.N. Agbor, A.C. Lopez, L.E. Nfonsam, S.S. Bornstein, M.A. Handel, and C.C. Linder. 2013. New point mutation in Golga3 causes multiple defects in spermatogenesis. *Andrology*. 1:440-450.

Bergen, D.J.M., N.L. Stevenson, R.E.H. Skinner, D.J. Stephens, and C.L. Hammond. 2017. The Golgi matrix protein giantin is required for normal cilia function in zebrafish. *Biol Open*. 6:1180-1189.

Bird, I.M., S.H. Kim, D.K. Schweppe, J. Caetano-Lopes, A.G. Robling, J.F. Charles, S.P. Gygi, M.L. Warman, and P.J. Smits. 2018. The skeletal phenotype of achondrogenesis type 1A is caused exclusively by cartilage defects. *Development*. 145.

Boncompain, G., L. Fourriere, N. Gareil, and F. Perez. 2021. Retention Using Selective Hooks-Synchronized Secretion to Measure Local Exocytosis. *Methods Mol Biol*. 2233:253-264.

Chang, W.L., C.W. Chang, Y.Y. Chang, H.H. Sung, M.D. Lin, S.C. Chang, C.H. Chen, C.W. Huang, K.S. Tung, and T.B. Chou. 2013. The Drosophila GOLPH3 homolog regulates the biosynthesis of heparan sulfate proteoglycans by modulating the retrograde trafficking of exostosins. *Development*. 140:2798-2807.

Costantini, A., H. Valta, A.M. Suomi, O. Makitie, and F. Taylan. 2021. Oligogenic Inheritance of Monoallelic TRIP11, FKBP10, NEK1, TBX5, and NBAS Variants Leading to a Phenotype Similar to Odontochondrodysplasia. *Front Genet*. 12:680838.

Couchman, J.R., and C.A. Pataki. 2012. An introduction to proteoglycans and their localization. *J Histochem Cytochem*. 60:885-897.

Del Pino, M., M.J. Sanchez-Soler, M. Parron-Pajares, M. Aza-Carmona, K.E. Heath, and V. Fano. 2021. Description of four patients with TRIP11 variants expand the clinical spectrum of odontochondroplasia (ODCD) and demonstrate the existence of common variants. *Eur J Med Genet*. 64:104198.

Follit, J.A., J.T. San Agustin, F. Xu, J.A. Jonassen, R. Samtani, C.W. Lo, and G.J. Pazour. 2008. The Golgin GMAP210/TRIP11 anchors IFT20 to the Golgi complex. *PLoS Genet*. 4:e1000315.

1112 Gandhi, N.S., and R.L. Mancera. 2008. The structure of glycosaminoglycans and their interactions
1113 with proteins. *Chem Biol Drug Des*. 72:455-482.
1114 Gillingham, A.K., and S. Munro. 2016. Finding the Golgi: Golgin Coiled-Coil Proteins Show the Way.
1115 *Trends Cell Biol*. 26:399-408.
1116 Guinec, N., V. Dalet-Fumeron, and M. Pagano. 1993. "In vitro" study of basement membrane
1117 degradation by the cysteine proteinases, cathepsins B, B-like and L. Digestion of collagen IV,
1118 laminin, fibronectin, and release of gelatinase activities from basement membrane
1119 fibronectin. *Biol Chem Hoppe Seyler*. 374:1135-1146.
1120 Harada, A., M. Kunii, K. Kurokawa, T. Sumi, S. Kanda, Y. Zhang, S. Nadanaka, K.M. Hirosawa, K.
1121 Tokunaga, T. Tojima, M. Taniguchi, K. Moriwaki, S.I. Yoshimura, M. Yamamoto-Hino, S. Goto,
1122 T. Katagiri, S. Kume, M. Hayashi-Nishino, M. Nakano, E. Miyoshi, K.G.N. Suzuki, H. Kitagawa,
1123 and A. Nakano. 2024. Dynamic movement of the Golgi unit and its glycosylation enzyme
1124 zones. *Nat Commun*. 15:4514.
1125 Hellicar, J., N.L. Stevenson, D.J. Stephens, and M. Lowe. 2022. Supply chain logistics - the role of the
1126 Golgi complex in extracellular matrix production and maintenance. *J Cell Sci*. 135.
1127 Hicks, S.W., T.A. Horn, J.M. McCaffery, D.M. Zuckerman, and C.E. Machamer. 2006. Golgin-160
1128 promotes cell surface expression of the beta-1 adrenergic receptor. *Traffic*. 7:1666-1677.
1129 Hicks, S.W., and C.E. Machamer. 2005. Isoform-specific interaction of golgin-160 with the Golgi-
1130 associated protein PIST. *J Biol Chem*. 280:28944-28951.
1131 Jangra, J., N.G. Bajad, R. Singh, A. Kumar, and S.K. Singh. 2024. Identification of novel potential
1132 cathepsin-B inhibitors through pharmacophore-based virtual screening, molecular docking,
1133 and dynamics simulation studies for the treatment of Alzheimer's disease. *Mol Divers*.
1134 Karamanos, N.K., A.D. Theocharis, Z. Piperigkou, D. Manou, A. Passi, S.S. Skandalis, D.H. Vynios, V.
1135 Orian-Rousseau, S. Ricard-Blum, C.E.H. Schmelzer, L. Duca, M. Durbeej, N.A. Afratis, L.
1136 Troeberg, M. Franchi, V. Masola, and M. Onisto. 2021. A guide to the composition and
1137 functions of the extracellular matrix. *FEBS J*. 288:6850-6912.
1138 Katayama, K., M. Kuriki, T. Kamiya, Y. Tochigi, and H. Suzuki. 2018. Giantin is required for coordinated
1139 production of aggrecan, link protein and type XI collagen during chondrogenesis. *Biochem*
1140 *Biophys Res Commun*. 499:459-465.
1141 Katayama, K., T. Sasaki, S. Goto, K. Ogasawara, H. Maru, K. Suzuki, and H. Suzuki. 2011. Insertional
1142 mutation in the Golgb1 gene is associated with osteochondrodysplasia and systemic edema
1143 in the OCD rat. *Bone*. 49:1027-1036.
1144 Kikukawa, K., T. Kamei, and K. Suzuki. 1991a. Chromatographic analysis of glycosaminoglycans in
1145 epiphyseal cartilage of congenital osteochondrodysplasia (ocd/ocd) rat. *J Vet Med Sci*.
1146 53:1091-1092.
1147 Kikukawa, K., T. Kamei, and K. Suzuki. 1991b. A histological and histochemical study on
1148 glycosaminoglycans in epiphysial cartilage of osteochondrodysplasia rat (OCD/OCD). *Connect*
1149 *Tissue Res*. 25:301-309.
1150 Kikukawa, K., T. Kamei, K. Suzuki, and K. Maita. 1990. Electron microscopic observations and
1151 electrophoresis of the glycosaminoglycans in the epiphyseal cartilage of the congenital
1152 osteochondrodysplasia rat (ocd/ocd). *Matrix*. 10:378-387.
1153 Kikukawa, K., and K. Suzuki. 1992. Histochemical and immunohistochemical distribution of
1154 glycosaminoglycans, type II collagen, and fibronectin in developing fetal cartilage of
1155 congenital osteochondrodysplasia rat (ocd/ocd). *Teratology*. 46:509-523.
1156 Kramer, A., J. Green, J. Pollard, Jr., and S. Tugendreich. 2014. Causal analysis approaches in Ingenuity
1157 Pathway Analysis. *Bioinformatics*. 30:523-530.
1158 Lan, Y., N. Zhang, H. Liu, J. Xu, and R. Jiang. 2016. Golgb1 regulates protein glycosylation and is crucial
1159 for mammalian palate development. *Development*. 143:2344-2355.
1160 Lazaro-Dieguez, F., N. Jimenez, H. Barth, A.J. Koster, J. Renau-Piqueras, J.L. Llopis, K.N. Burger, and G.
1161 Egea. 2006. Actin filaments are involved in the maintenance of Golgi cisternae morphology
1162 and intra-Golgi pH. *Cell Motil Cytoskeleton*. 63:778-791.

1163 Lee, M.H., and G. Murphy. 2004. Matrix metalloproteinases at a glance. *J Cell Sci*. 117:4015-4016.
1164 Lohmander, S., K. Madsen, and A. Hinek. 1979. Secretion of proteoglycans by chondrocytes.
1165 Influence of colchicine, cytochalasin B, and beta-D-xyloside. *Arch Biochem Biophys*. 192:148-
1166 157.
1167 Lowe, M. 2011. Structural organization of the Golgi apparatus. *Curr Opin Cell Biol*. 23:85-93.
1168 Lowe, M. 2019. The Physiological Functions of the Golgin Vesicle Tethering Proteins. *Front Cell Dev*
1169 *Biol*. 7:94.
1170 Matsukuma, S., M. Kondo, M. Yoshihara, M. Matsuda, T. Utakoji, and S. Sutou. 1999. Mea2/Golga3
1171 gene is disrupted in a line of transgenic mice with a reciprocal translocation between
1172 Chromosomes 5 and 19 and is responsible for a defective spermatogenesis in homozygotes.
1173 *Mamm Genome*. 10:1-5.
1174 McCaughey, J., N.L. Stevenson, S. Cross, and D.J. Stephens. 2019. ER-to-Golgi trafficking of
1175 procollagen in the absence of large carriers. *J Cell Biol*. 218:929-948.
1176 McCaughey, J., N.L. Stevenson, J.M. Mantell, C.R. Neal, A. Paterson, K. Heesom, and D.J. Stephens.
1177 2021. A general role for TANGO1, encoded by MIA3, in secretory pathway organization and
1178 function. *J Cell Sci*. 134.
1179 Medina, C.T.N., R. Sandoval, G. Oliveira, K. da Costa Silveira, D.P. Cavalcanti, and R. Pogue. 2020.
1180 Pathogenic variants in the TRIP11 gene cause a skeletal dysplasia spectrum from
1181 odontochondrodysplasia to achondrogenesis 1A. *Am J Med Genet A*. 182:681-688.
1182 Pascovici, D., D.C. Handler, J.X. Wu, and P.A. Haynes. 2016. Multiple testing corrections in quantitative
1183 proteomics: A useful but blunt tool. *Proteomics*. 16:2448-2453.
1184 Podgorski, I., B.E. Linebaugh, J.E. Koblinski, D.L. Rudy, M.K. Herroon, M.B. Olive, and B.F. Sloane.
1185 2009. Bone marrow-derived cathepsin K cleaves SPARC in bone metastasis. *Am J Pathol*.
1186 175:1255-1269.
1187 Potelle, S., A. Klein, and F. Foulquier. 2015. Golgi post-translational modifications and associated
1188 diseases. *J Inherit Metab Dis*. 38:741-751.
1189 Qian, Y., G. Hu, M. Chen, B. Liu, K. Yan, C. Zhou, Y. Yu, and M. Dong. 2021. Novel deep intronic and
1190 frameshift mutations causing a TRIP11-related disorder. *Am J Med Genet A*. 185:2482-2487.
1191 Rabouille, C., N. Hui, F. Hunte, R. Kieckbusch, E.G. Berger, G. Warren, and T. Nilsson. 1995. Mapping
1192 the distribution of Golgi enzymes involved in the construction of complex oligosaccharides. *J*
1193 *Cell Sci*. 108 (Pt 4):1617-1627.
1194 Ricard-Blum, S., R.R. Vives, L. Schaefer, M. Gotte, R. Merline, A. Passi, P. Heldin, A. Magalhaes, C.A.
1195 Reis, S.S. Skandalis, N.K. Karamanos, S. Perez, and D. Nikitovic. 2024. A biological guide to
1196 glycosaminoglycans: current perspectives and pending questions. *FEBS J*. 291:3331-3366.
1197 Sato, K., P. Roboti, A.A. Mironov, and M. Lowe. 2015. Coupling of vesicle tethering and Rab binding is
1198 required for in vivo functionality of the golgin GMAP-210. *Mol Biol Cell*. 26:537-553.
1199 Shao, X., C.D. Gomez, N. Kapoor, J.M. Considine, C. Grams, Y.T. Gao, and A. Naba. 2023. MatrisomeDB
1200 2.0: 2023 updates to the ECM-protein knowledge database. *Nucleic Acids Res*. 51:D1519-
1201 D1530.
1202 Smits, P., A.D. Bolton, V. Funari, M. Hong, E.D. Boyden, L. Lu, D.K. Manning, N.D. Dwyer, J.L. Moran,
1203 M. Prysak, B. Merriman, S.F. Nelson, L. Bonafe, A. Superti-Furga, S. Ikegawa, D. Krakow, D.H.
1204 Cohn, T. Kirchhausen, M.L. Warman, and D.R. Beier. 2010. Lethal skeletal dysplasia in mice
1205 and humans lacking the golgin GMAP-210. *N Engl J Med*. 362:206-216.
1206 Stevenson, N.L., D.J.M. Bergen, Y. Lu, M.E. Prada-Sanchez, K.E. Kadler, C.L. Hammond, and D.J.
1207 Stephens. 2021. Giantin is required for intracellular N-terminal processing of type I
1208 procollagen. *J Cell Biol*. 220.
1209 Stevenson, N.L., D.J.M. Bergen, R.E.H. Skinner, E. Kague, E. Martin-Silverstone, K.A. Robson Brown,
1210 C.L. Hammond, and D.J. Stephens. 2017. Giantin-knockout models reveal a feedback loop
1211 between Golgi function and glycosyltransferase expression. *J Cell Sci*. 130:4132-4143.

Suzuki, K., K. Kikukawa, Y. Hakamata, T. Kamei, and T. Imamichi. 1988. Congenital osteochondrodysplasia with systemic subcutaneous edema (ocd/ocd): a new lethal autosomal recessive mutant of the rat. *J Hered*. 79:48-50.

Tie, H.C., D. Mahajan, and L. Lu. 2022. Visualizing intra-Golgi localization and transport by side-averaging Golgi ministacks. *J Cell Biol*. 221.

Upadhyai, P., P. Radhakrishnan, V.S. Guleria, N. Kausthubham, S.S. Nayak, A. Superti-Furga, and K.M. Girisha. 2021. Biallelic deep intronic variant c.5457+81T>A in TRIP11 causes loss of function and results in achondrogenesis 1A. *Hum Mutat*. 42:1005-1014.

Vidak, E., U. Javorsek, M. Vizovisek, and B. Turk. 2019. Cysteine Cathepsins and their Extracellular Roles: Shaping the Microenvironment. *Cells*. 8.

Vizovisek, M., M. Fonovic, and B. Turk. 2019. Cysteine cathepsins in extracellular matrix remodeling: Extracellular matrix degradation and beyond. *Matrix Biol*. 75-76:141-159.

Waldo, G.S., B.M. Standish, J. Berendzen, and T.C. Terwilliger. 1999. Rapid protein-folding assay using green fluorescent protein. *Nat Biotechnol*. 17:691-695.

Wehrle, A., T.M. Witkos, S. Unger, J. Schneider, J.A. Follit, J. Hermann, T. Welting, V. Fano, M. Hietala, N. Vatanavicharn, K. Schoner, J. Spranger, M. Schmidts, B. Zabel, G.J. Pazour, A. Bloch-Zupan, G. Nishimura, A. Superti-Furga, M. Lowe, and E. Lausch. 2019. Hypomorphic mutations of TRIP11 cause odontochondrodysplasia. *JCI Insight*. 4.

Wershof, E., D. Park, D.J. Barry, R.P. Jenkins, A. Rullan, A. Wilkins, K. Schlegelmilch, I. Roxanis, K.I. Anderson, P.A. Bates, and E. Sahai. 2021. A FIJI macro for quantifying pattern in extracellular matrix. *Life Sci Alliance*. 4.

Williams, D., S.W. Hicks, C.E. Machamer, and J.E. Pessin. 2006. Golgin-160 is required for the Golgi membrane sorting of the insulin-responsive glucose transporter GLUT4 in adipocytes. *Mol Biol Cell*. 17:5346-5355.

Witkos, T.M., and M. Lowe. 2015. The Golgin Family of Coiled-Coil Tethering Proteins. *Front Cell Dev Biol*. 3:86.

Wong, M., A.K. Gillingham, and S. Munro. 2017. The golgin coiled-coil proteins capture different types of transport carriers via distinct N-terminal motifs. *BMC Biol*. 15:3.

Wong, M., and S. Munro. 2014. Membrane trafficking. The specificity of vesicle traffic to the Golgi is encoded in the golgin coiled-coil proteins. *Science*. 346:1256898.

Yadav, S., M.A. Puthenveedu, and A.D. Linstedt. 2012. Golgin160 recruits the dynein motor to position the Golgi apparatus. *Dev Cell*. 23:153-165.

Yamaguchi, H., M.D. Meyer, L. He, and Y. Komatsu. 2022. Disruption of Trip11 in cranial neural crest cells is associated with increased ER and Golgi stress contributing to skull defects in mice. *Dev Dyn*. 251:1209-1222.

Yamaguchi, H., M.D. Meyer, L. He, L. Senavirathna, S. Pan, and Y. Komatsu. 2021. The molecular complex of ciliary and golgin protein is crucial for skull development. *Development*. 148.

Yeter, B., A. Dilruba Aslanger, G. Yesil, and N.H. Elcioglu. 2022. A Novel Mutation in the TRIP11 Gene: Diagnostic Approach from Relatively Common Skeletal Dysplasias to an Extremely Rare Odontochondrodysplasia. *J Clin Res Pediatr Endocrinol*. 14:475-480.

Zhang, X., and Y. Wang. 2016. Glycosylation Quality Control by the Golgi Structure. *J Mol Biol*. 428:3183-3193.

Figure 1

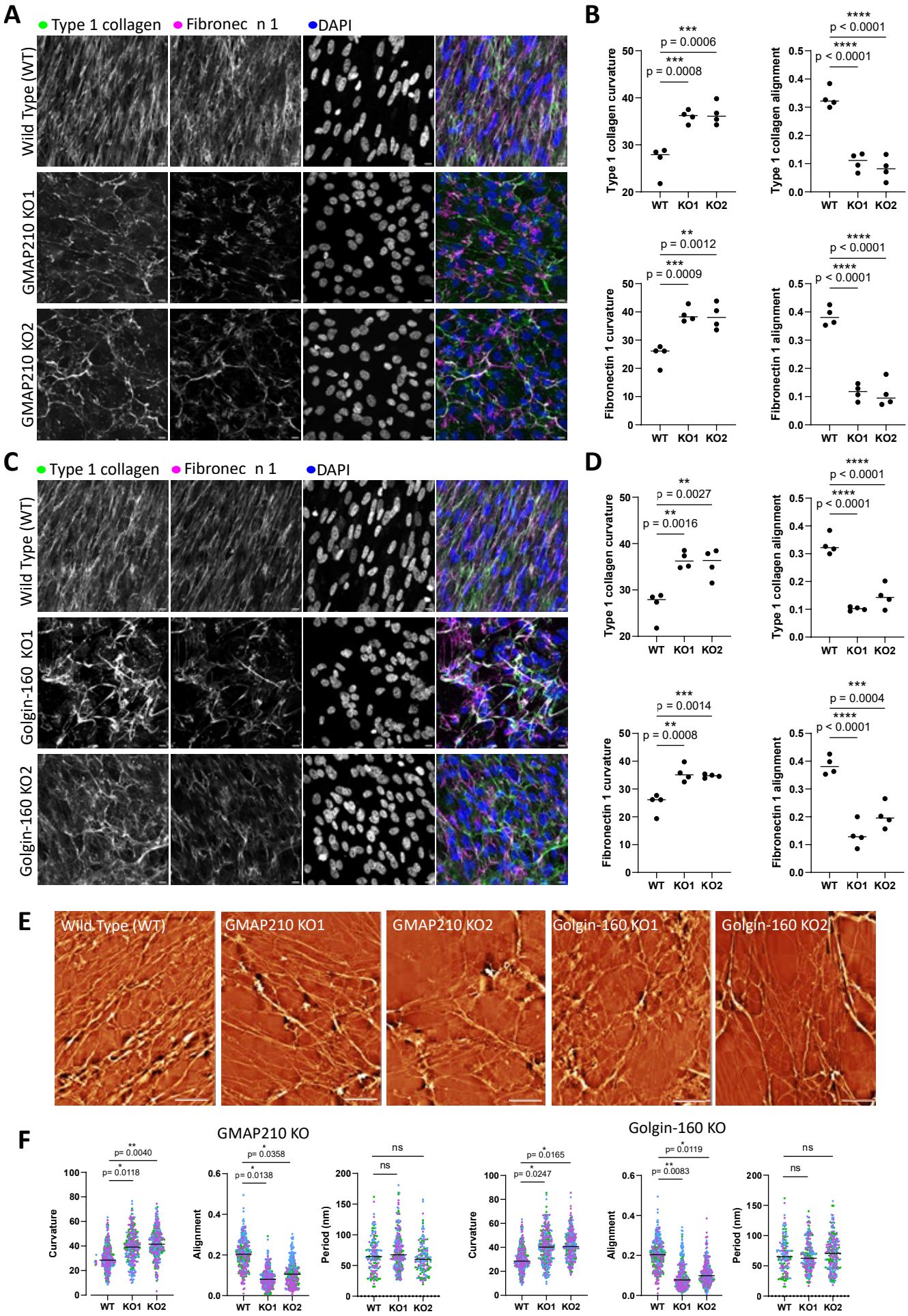
A
Type 1 collagen
Fibronec n 1
DAPI
Wild Type (WT)
GMAP210 KO1
GMAP210 KO2
B
Type 1 collagen curvature
Type 1 collagen alignment
Fibronectin 1 curvature
Fibronectin 1 alignment
WT KO1 KO2
C
Type 1 collagen
Fibronec n 1
DAPI
Wild Type (WT)
Golgin-160 KO1
Golgin-160 KO2
D
Type 1 collagen curvature
Type 1 collagen alignment
Fibronectin 1 curvature
Fibronectin 1 alignment
WT KO1 KO2
E
Wild Type (WT)
GMAP210 KO1
GMAP210 KO2
Golgin-160 KO1
Golgin-160 KO2
F
GMAP210 KO
Golgin-160 KO
Curvature
Alignment
Period (nm)
WT KO1 KO2

Figure 2

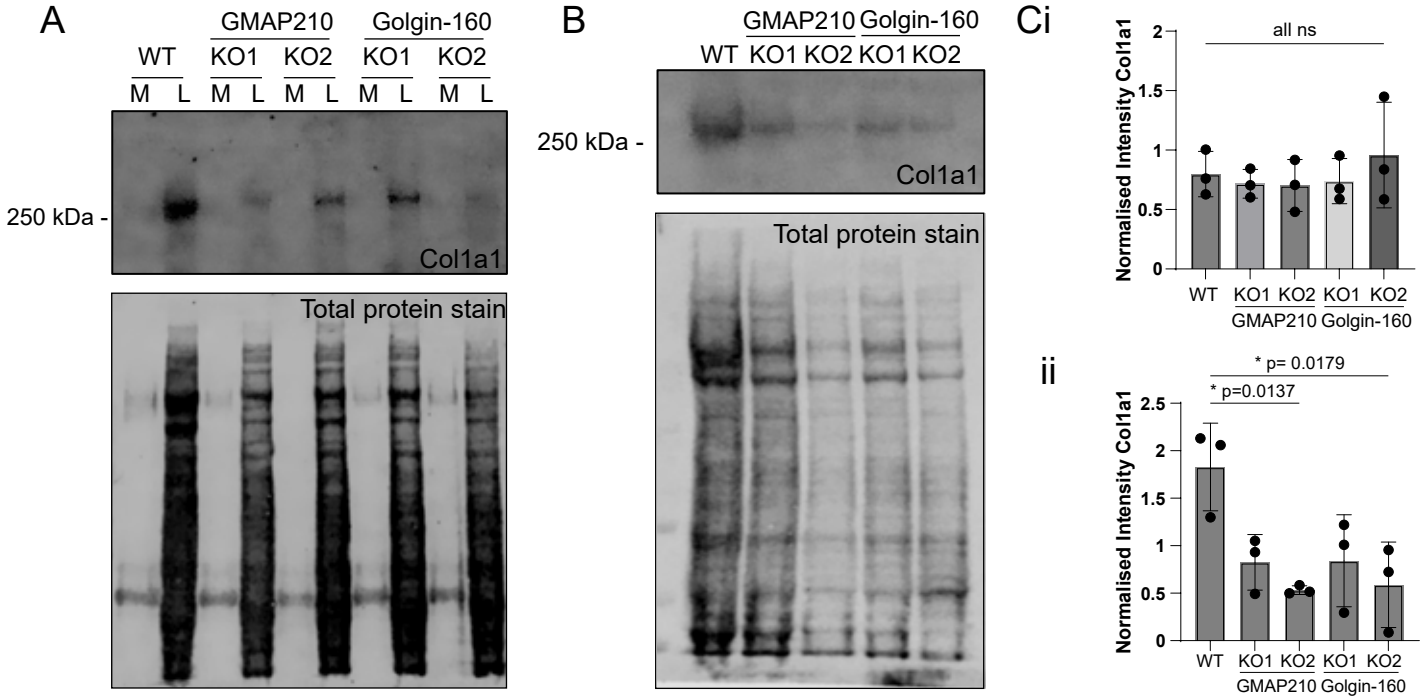
A
GMAP210
Golgin-160
WT
KO1
KO2
KO1
KO2
M L M L M L M L M L
250 kDa -
Col1a1
Total protein stain
B
GMAP210 Golgin-160
WT KO1 KO2 KO1 KO2
250 kDa -
Col1a1
Total protein stain
Ci
all ns
Normalised Intensity Col1a1
2
1.5
1
0.5
0
WT KO1 KO2 KO1 KO2
GMAP210 Golgin-160
ii
* p= 0.0179
* p=0.0137
Normalised Intensity Col1a1
2.5
2
1.5
1
0.5
0
WT KO1 KO2 KO1 KO2
GMAP210 Golgin-160

Figure 3

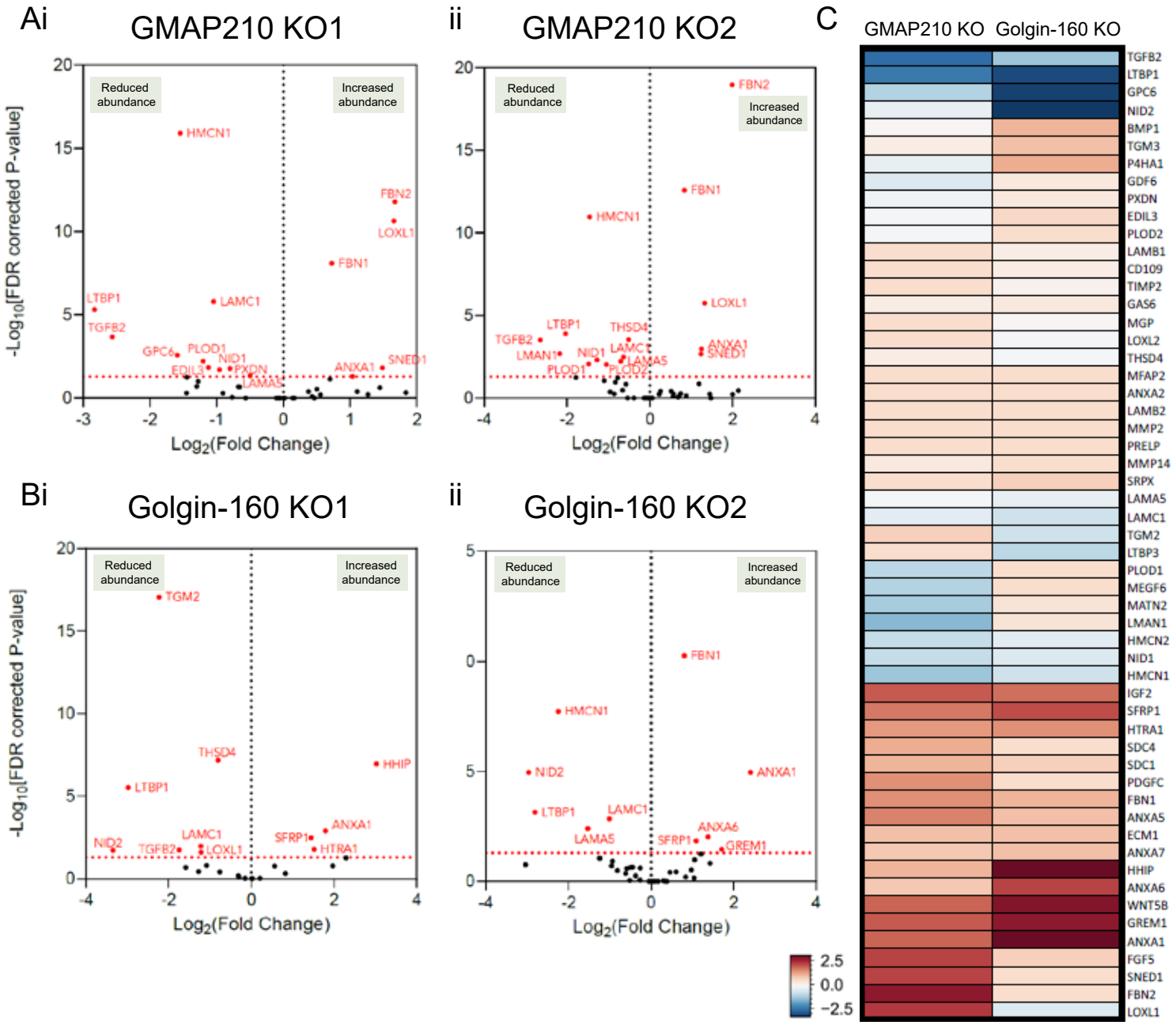
Ai
GMAP210 KO1
Reduced abundance
Increased abundance
HMCN1
FBN2
LOXL1
FBN1
LTBP1
LAMC1
TGFB2
GPC6
PLOD1
NID1
EDIL3
PXDN
LAMA5
ANXA1
SNED1
-Log10[FDR corrected P-value]
Log2(Fold Change)
ii
GMAP210 KO2
Reduced abundance
Increased abundance
FBN2
FBN1
HMCN1
LOXL1
LTBP1
THSD4
TGFB2
LMAN1
NID1
LAMC1
LAMA5
PLOD1
PLOD2
ANXA1
SNED1
Log2(Fold Change)
Bi
Golgin-160 KO1
Reduced abundance
Increased abundance
TGM2
THSD4
HHIP
LTBP1
NID2
TGFB2
LAMC1
LOXL1
SFRP1
ANXA1
HTRA1
-Log10[FDR corrected P-value]
Log2(Fold Change)
ii
Golgin-160 KO2
Reduced abundance
Increased abundance
FBN1
HMCN1
NID2
ANXA1
LTBP1
LAMC1
LAMA5
SFRP1
ANXA6
GREM1
Log2(Fold Change)
2.5
0.0
−2.5
C
GMAP210 KO
Golgin-160 KO
TGFB2
LTBP1
GPC6
NID2
BMP1
TGM3
P4HA1
GDF6
PXDN
EDIL3
PLOD2
LAMB1
CD109
TIMP2
GAS6
MGP
LOXL2
THSD4
MFAP2
ANXA2
LAMB2
MMP2
PRELP
MMP14
SRPX
LAMA5
LAMC1
TGM2
LTBP3
PLOD1
MEGF6
MATN2
LMAN1
HMCN2
NID1
HMCN1
IGF2
SFRP1
HTRA1
SDC4
SDC1
PDGFC
FBN1
ANXA5
ECM1
ANXA7
HHIP
ANXA6
WNT5B
GREM1
ANXA1
FGF5
SNED1
FBN2
LOXL1

Figure 4

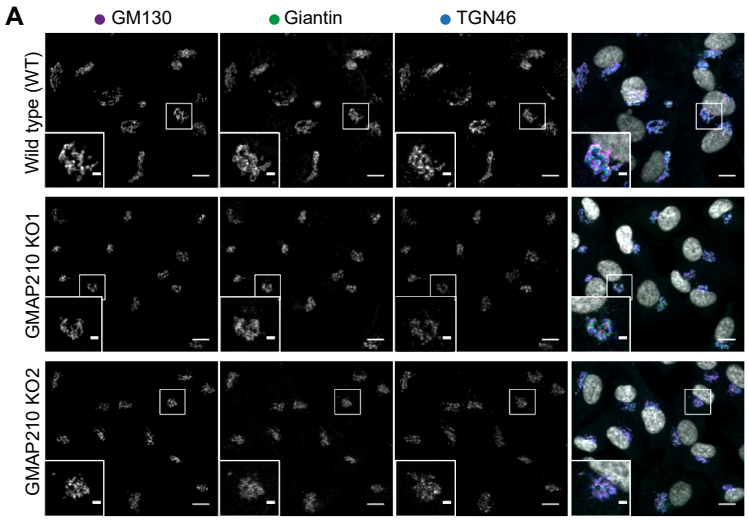
A
GM130
Giantin
TGN46
Wild type (WT)
GMAP210 KO1
GMAP210 KO2

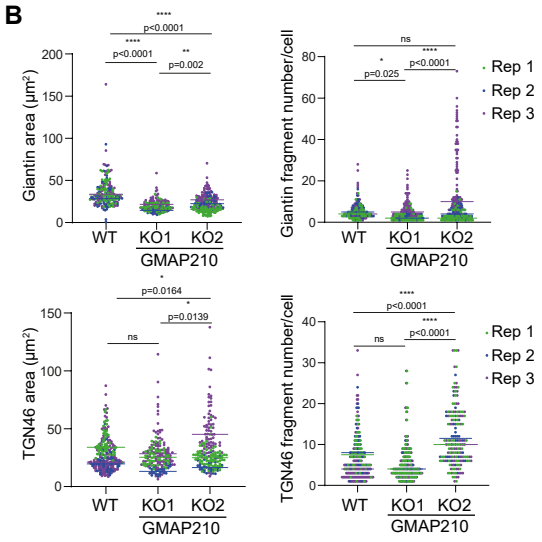
B
Giantin area (µm²)
Giantin fragment number/cell
TGN46 area (µm²)
TGN46 fragment number/cell
WT
KO1
KO2
GMAP210
Rep 1
Rep 2
Rep 3

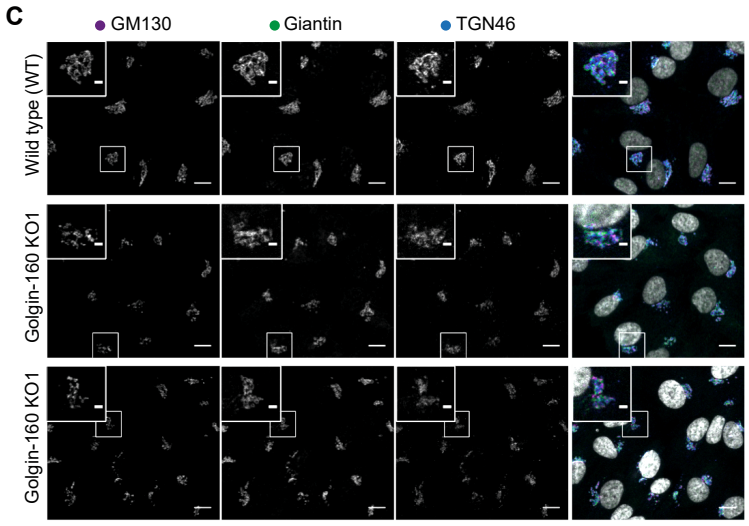
C
GM130
Giantin
TGN46
Wild type (WT)
Golgin-160 KO1
Golgin-160 KO1

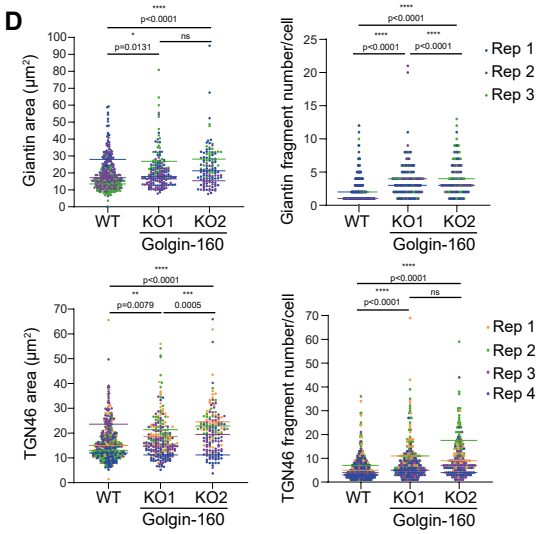
D
Giantin area (µm²)
Giantin fragment number/cell
TGN46 area (µm²)
TGN46 fragment number/cell
WT
KO1
KO2
Golgin-160
Rep 1
Rep 2
Rep 3
Rep 4

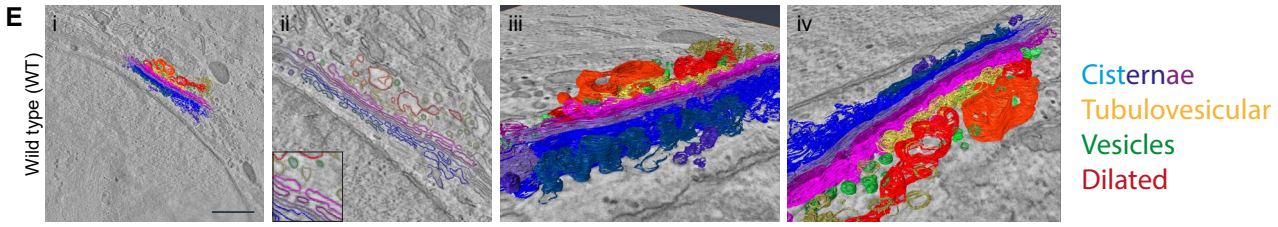
E
Wild type (WT)
i
ii
iii
iv
Cisternae
Tubulovesicular
Vesicles
Dilated

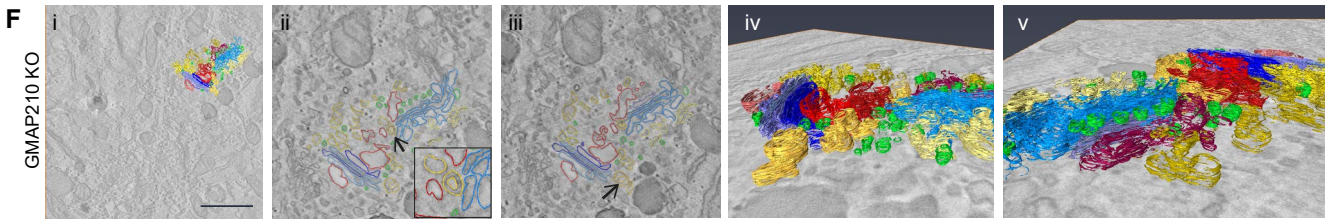
F
GMAP210 KO
i
ii
iii
iv
v

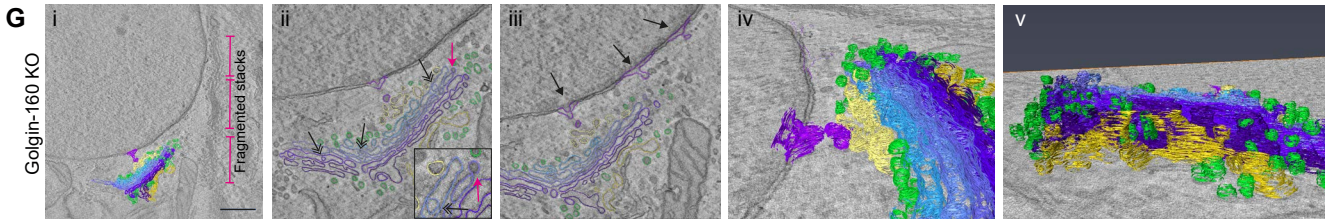
G
Golgin-160 KO
i
ii
iii
iv
v
Fragmented stacks

Figure 5

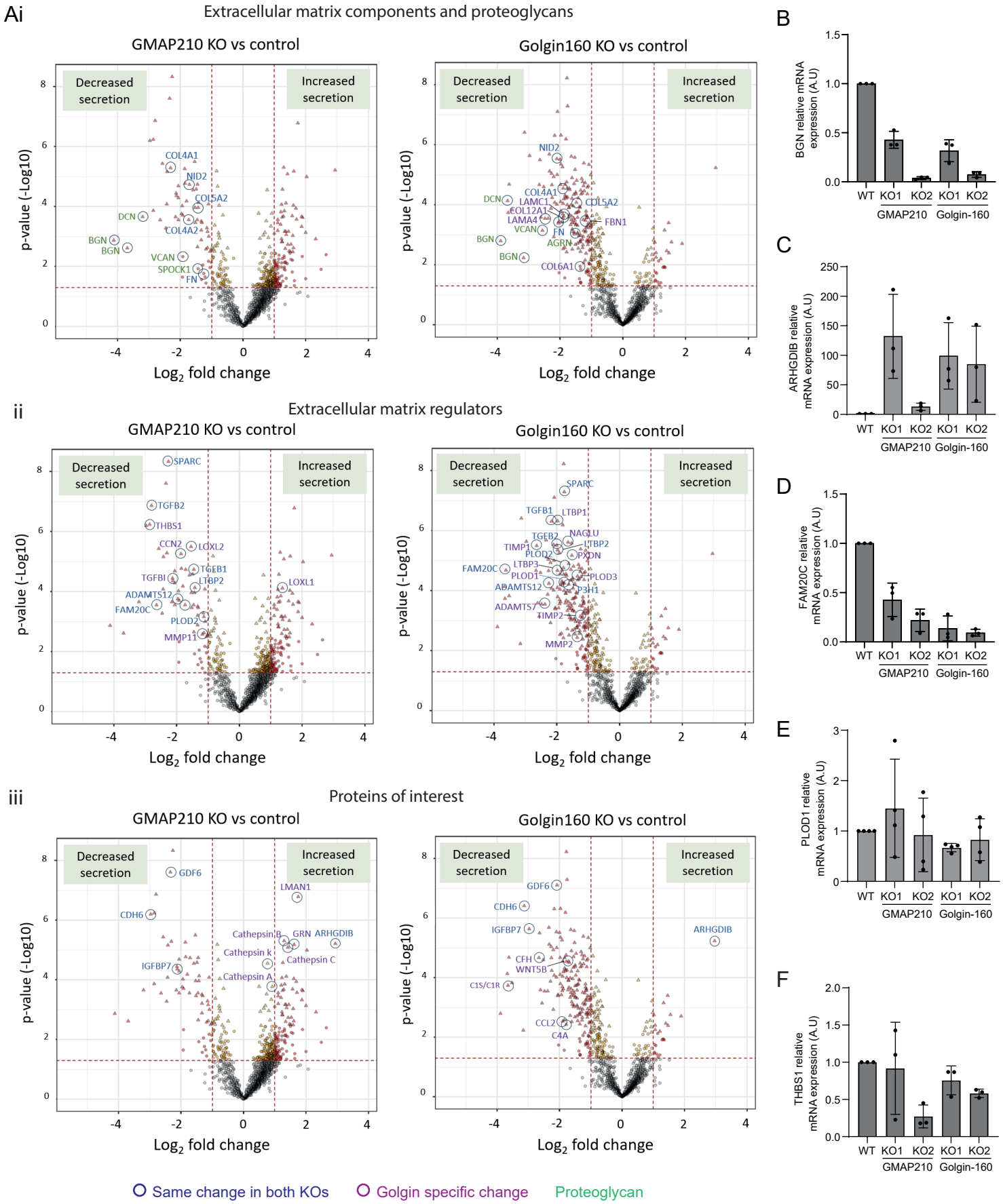
Ai
Extracellular matrix components and proteoglycans
GMAP210 KO vs control
Golgin160 KO vs control
Decreased secretion
Increased secretion
p-value (-Log10)
Log2 fold change
COL4A1
NID2
COL5A2
DCN
COL4A2
BGN
VCAN
SPOCK1
FN
LAMC1
COL12A1
LAMA4
FBN1
AGRN
COL6A1
ii
Extracellular matrix regulators
SPARC
TGFB2
THBS1
CCN2
LOXL2
TGFB1
TGFBI
LTBP2
LOXL1
ADAMTS12
FAM20C
PLOD2
MMP11
LTBP1
NAGLU
TIMP1
PXDN
LTBP3
PLOD1
PLOD3
P3H1
ADAMTS7
TIMP2
MMP2
iii
Proteins of interest
GDF6
LMAN1
CDH6
Cathepsin B
GRN
ARHGDIB
Cathepsin k
Cathepsin C
IGFBP7
Cathepsin A
CFH
WNT5B
C1S/C1R
CCL2
C4A
B
BGN relative mRNA expression (A.U)
C
ARHGDIB relative mRNA expression (A.U)
D
FAM20C relative mRNA expression (A.U)
E
PLOD1 relative mRNA expression (A.U)
F
THBS1 relative mRNA expression (A.U)
WT KO1 KO2 KO1 KO2
GMAP210 Golgin-160
Same change in both KOs
Golgin specific change
Proteoglycan

Figure 6

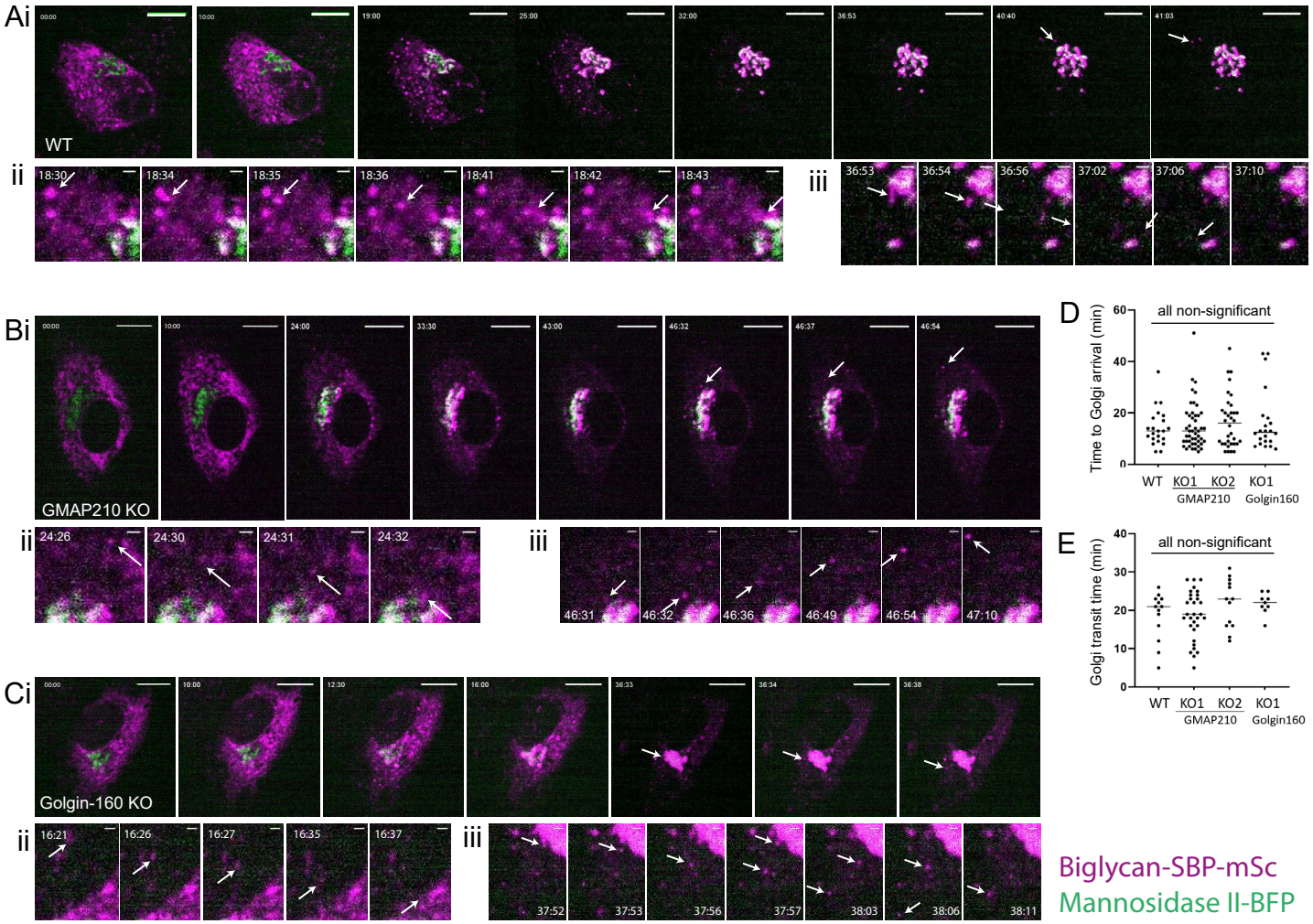
Ai
WT
ii
iii
Bi
GMAP210 KO
ii
iii
Ci
Golgin-160 KO
ii
iii
D
all non-significant
Time to Golgi arrival (min)
WT
KO1
KO2
KO1
GMAP210
Golgin160
E
all non-significant
Golgi transit time (min)
WT
KO1
KO2
KO1
GMAP210
Golgin160
Biglycan-SBP-mSc
Mannosidase II-BFP

Figure 7

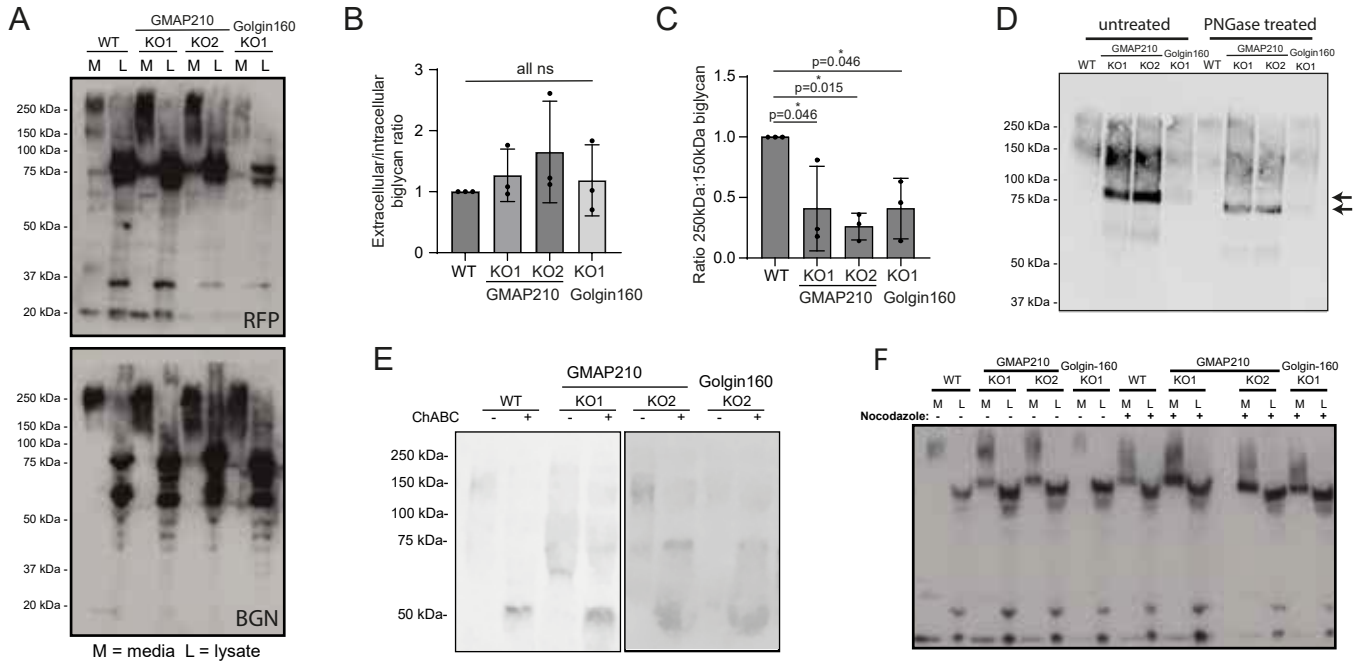
A
GMAP210
Golgin160
WT
KO1
KO2
KO1
M L M L M L M L
250 kDa
150 kDa
100 kDa
75 kDa
50 kDa
37 kDa
20 kDa
RFP
BGN
M = media L = lysate
B
all ns
Extracellular/intracellular biglycan ratio
WT KO1 KO2 KO1
GMAP210 Golgin160
C
p=0.046
p=0.015
p=0.046
Ratio 250kDa:150kDa biglycan
WT KO1 KO2 KO1
GMAP210 Golgin160
D
untreated
PNGase treated
GMAP210
Golgin160
WT KO1 KO2 KO1 WT KO1 KO2 KO1
250 kDa
150 kDa
100 kDa
75 kDa
50 kDa
37 kDa
E
GMAP210
Golgin160
WT
KO1
KO2
KO2
ChABC - + - + - + - +
250 kDa
150 kDa
100 kDa
75 kDa
50 kDa
F
GMAP210
Golgin-160
WT
KO1
KO2
KO1
WT
KO1
KO2
KO1
M L M L M L M L M L M L M L M L
Nocodazole: - - - - - - - - + + + + + + + +

Table 1 - GO term analysis of golgin secretome data

Golgin-160 KO cell secretome GO term analysis

Term	Count	%	PValue	List Total	Fold Enrichment	Bonferroni	Benjamini	FDR
GO:0007155~cell adhesion	41	16.4	3.80E-19	244	5.767643912	8.70E-16	8.70E-16	8.39E-16
GO:0030199~collagen fibril organization	17	6.8	1.52E-15	244	17.60985736	3.56E-12	1.75E-12	1.68E-12
GO:0030335~positive regulation of cell migration	20	8	1.16E-09	244	5.974703751	2.66E-06	8.88E-07	8.55E-07
GO:0030198~extracellular matrix organization	17	6.8	2.24E-09	244	7.136626402	5.13E-06	1.05E-06	1.01E-06
GO:0016477~cell migration	20	8	2.29E-09	244	5.73829461	5.25E-06	1.05E-06	1.01E-06
GO:0071711~basement membrane organization	7	2.8	2.25E-07	244	25.37891207	5.15E-04	8.59E-05	8.27E-05
GO:0007275~multicellular organism development	13	5.2	2.65E-07	244	7.20076275	6.07E-04	8.67E-05	8.36E-05
GO:0006508~proteolysis	22	8.8	3.31E-07	244	3.83137662	7.58E-04	9.48E-05	9.14E-05
GO:0002062~chondrocyte differentiation	9	3.6	4.46E-07	244	12.81894028	0.001021628	1.14E-04	1.09E-04
GO:0007179~transforming growth factor beta receptor signaling pathway	11	4.4	6.53E-07	244	8.518303358	0.001496695	1.50E-04	1.44E-04
GO:0006024~glycosaminoglycan biosynthetic process	8	3.2	1.12E-06	244	14.50223547	0.002567717	2.34E-04	2.25E-04
GO:0035987~endodermal cell differentiation	7	2.8	2.02E-06	244	18.01084082	0.004617163	3.86E-04	3.72E-04
GO:0030509~BMP signaling pathway	10	4	2.94E-06	244	8.396031061	0.006713032	5.18E-04	4.99E-04
GO:0051897~positive regulation of protein kinase B signaling	13	5.2	3.80E-06	244	5.604918033	0.00866714	6.22E-04	5.99E-04
GO:0043406~positive regulation of MAP kinase activity	9	3.6	5.27E-06	244	9.322865659	0.012012798	8.06E-04	7.76E-04

GMAP210 KO cell secretome GO term analysis

Term	Count	%	PValue	List Total	Fold Enrichment	Bonferroni	Benjamini	FDR
GO:0061644~protein localization to CENP-A containing chromatin	15	8.064516129	6.42E-26	182	89.11172161	1.07E-22	1.07E-22	1.05E-22
GO:0006336~DNA replication-independent nucleosome assembly	16	8.602150538	2.93E-24	182	63.36833537	4.88E-21	1.63E-21	1.60E-21
GO:0032200~telomere organization	16	8.602150538	2.93E-24	182	63.36833537	4.88E-21	1.63E-21	1.60E-21
GO:0045653~negative regulation of megakaryocyte differentiation	14	7.52688172	1.83E-22	182	74.85384615	3.06E-19	7.65E-20	7.51E-20
GO:0006335~DNA replication-dependent nucleosome assembly	14	7.52688172	7.41E-19	182	46.78365385	1.23E-15	2.47E-16	2.43E-16
GO:0006352~DNA-templated transcription, initiation	14	7.52688172	3.47E-17	182	36.51407129	5.79E-14	9.65E-15	9.49E-15
GO:0006334~nucleosome assembly	21	11.29032258	1.33E-16	182	13.13225371	1.85E-13	3.18E-14	3.12E-14
GO:0006325~chromatin organization	21	11.29032258	2.46E-11	182	6.952369612	4.10E-08	5.13E-09	5.04E-09
GO:0030199~collagen fibril organization	12	6.451612903	1.30E-10	182	16.66504924	2.17E-07	2.41E-08	2.37E-08
GO:0007155~cell adhesion	25	13.44086022	6.06E-10	182	4.714905905	1.01E-06	1.01E-07	9.93E-08
GO:0030198~extracellular matrix organization	12	6.451612903	1.71E-06	182	6.75373048	0.002841578	2.59E-04	2.54E-04
GO:0001649~osteoblast differentiation	10	5.376344086	3.15E-06	182	8.354223901	0.005229865	4.37E-04	4.29E-04
GO:0001666~response to hypoxia	11	5.913978495	6.35E-06	182	6.645619917	0.010532333	8.14E-04	8.00E-04
GO:0016477~cell migration	13	6.989247312	1.19E-05	182	5.000513875	0.019662423	0.001418442	0.001394
GO:0002062~chondrocyte differentiation	7	3.76344086	1.31E-05	182	13.36675824	0.02167745	0.001461048	0.001436
GO:0030335~positive regulation of cell migration	12	6.451612903	4.21E-05	182	4.806025435	0.067714253	0.004300498	0.004226

Supplemental Figure 1

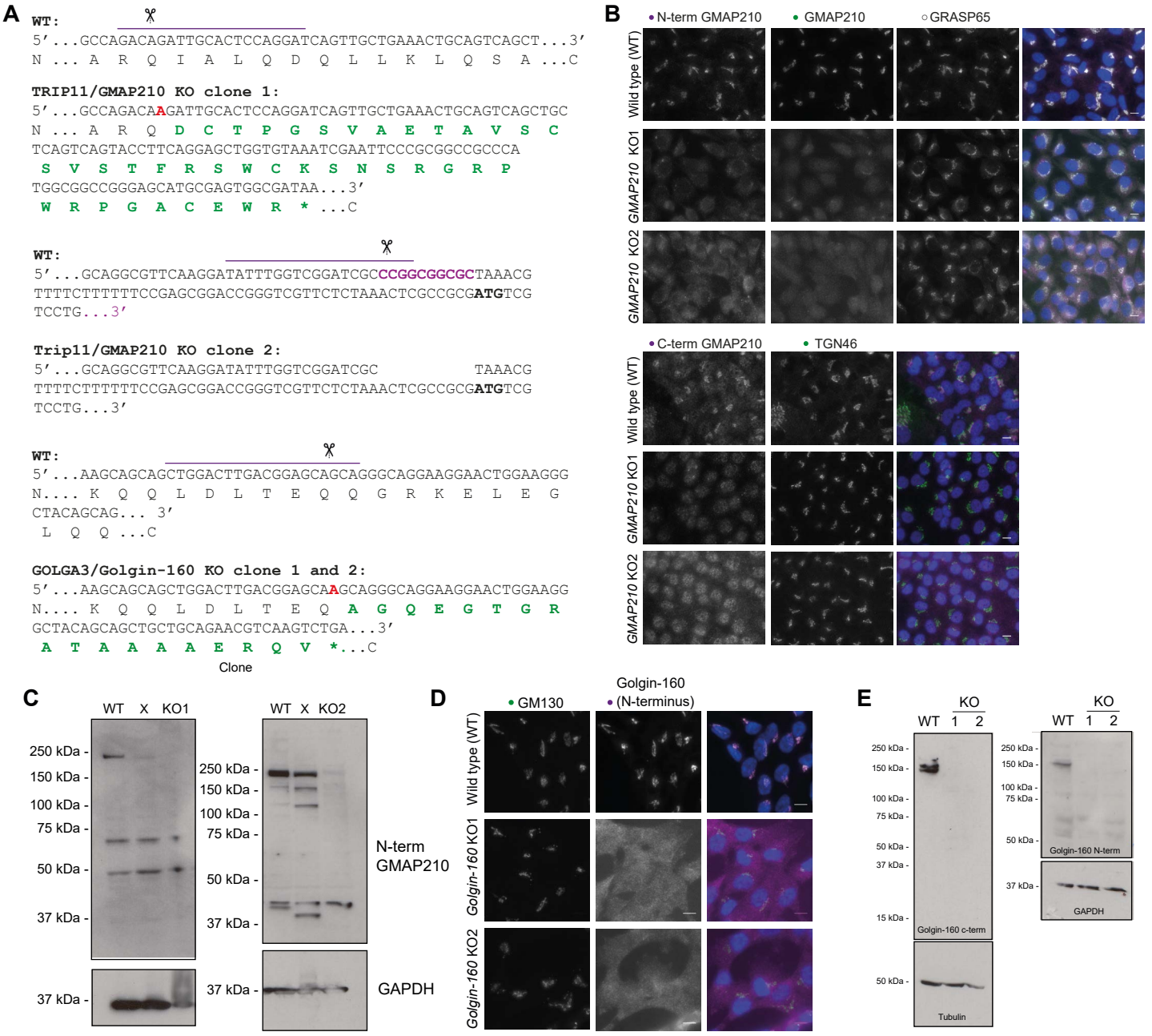

Supplemental Figure 2

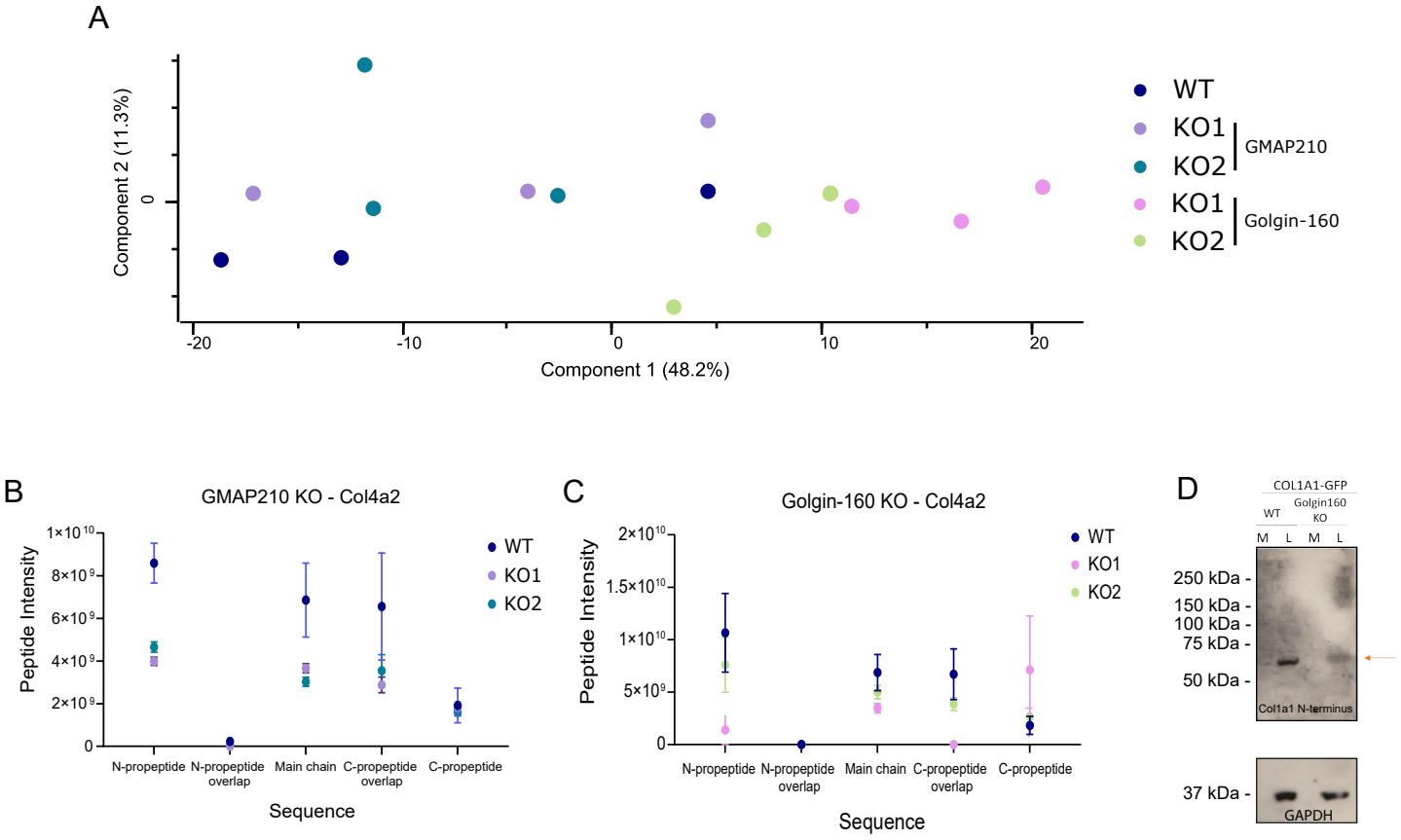

Supplemental Figure 3

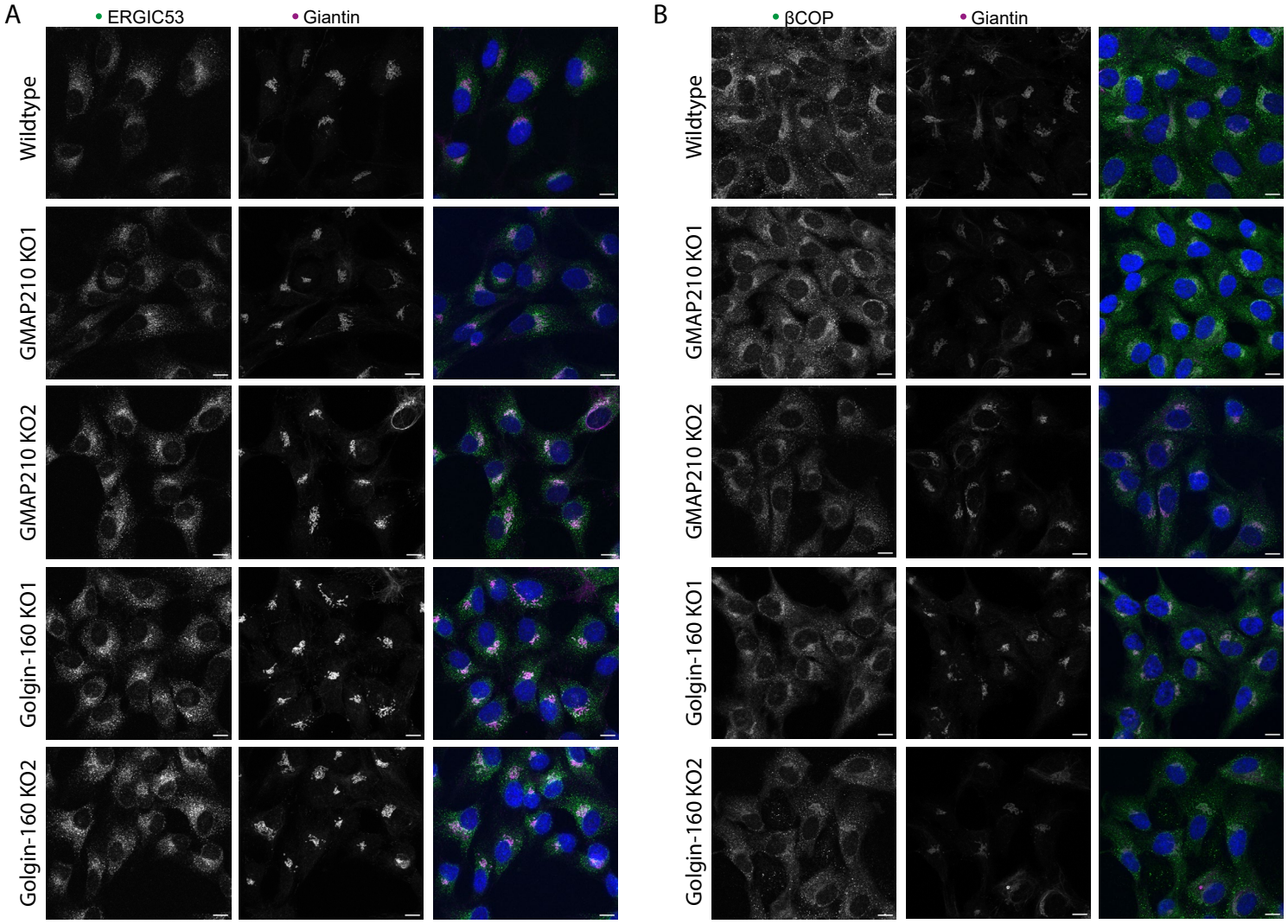

Supplemental Figure 4

A

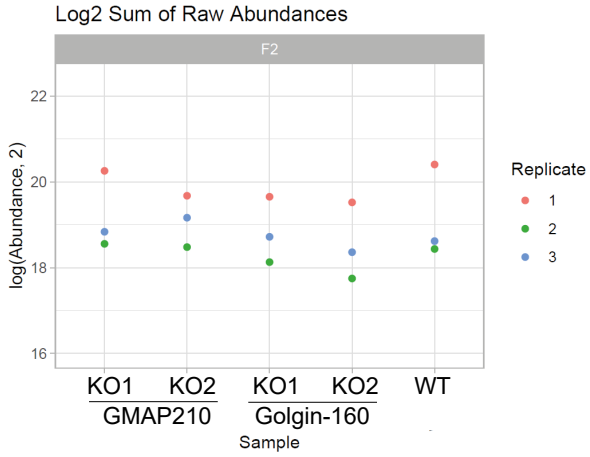

B

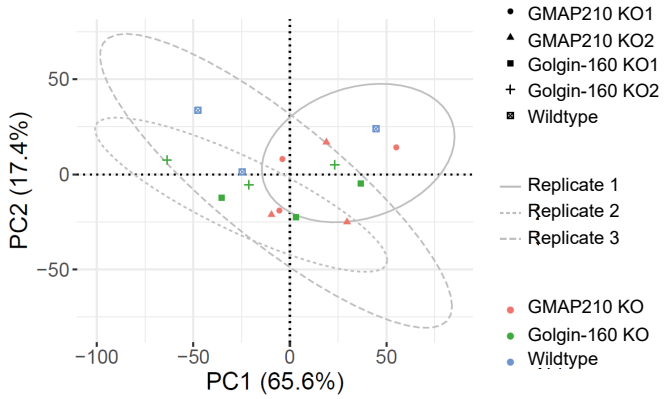

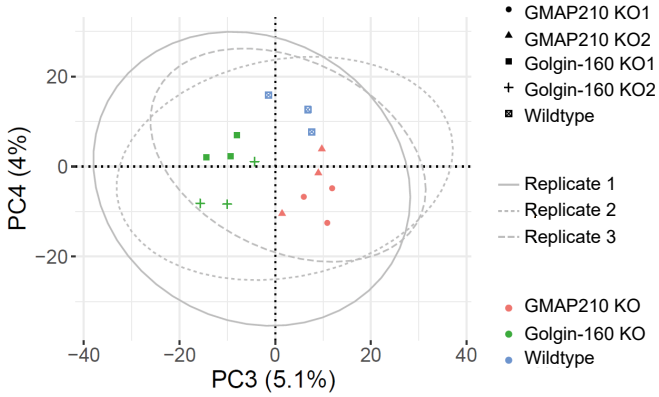

C

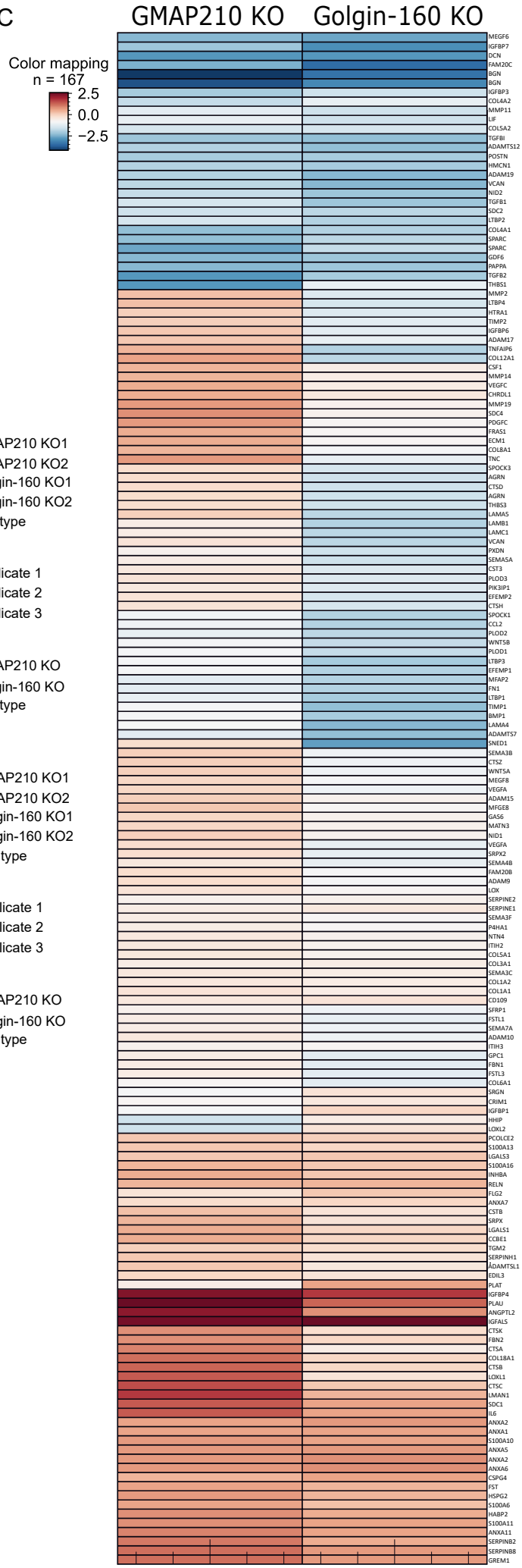
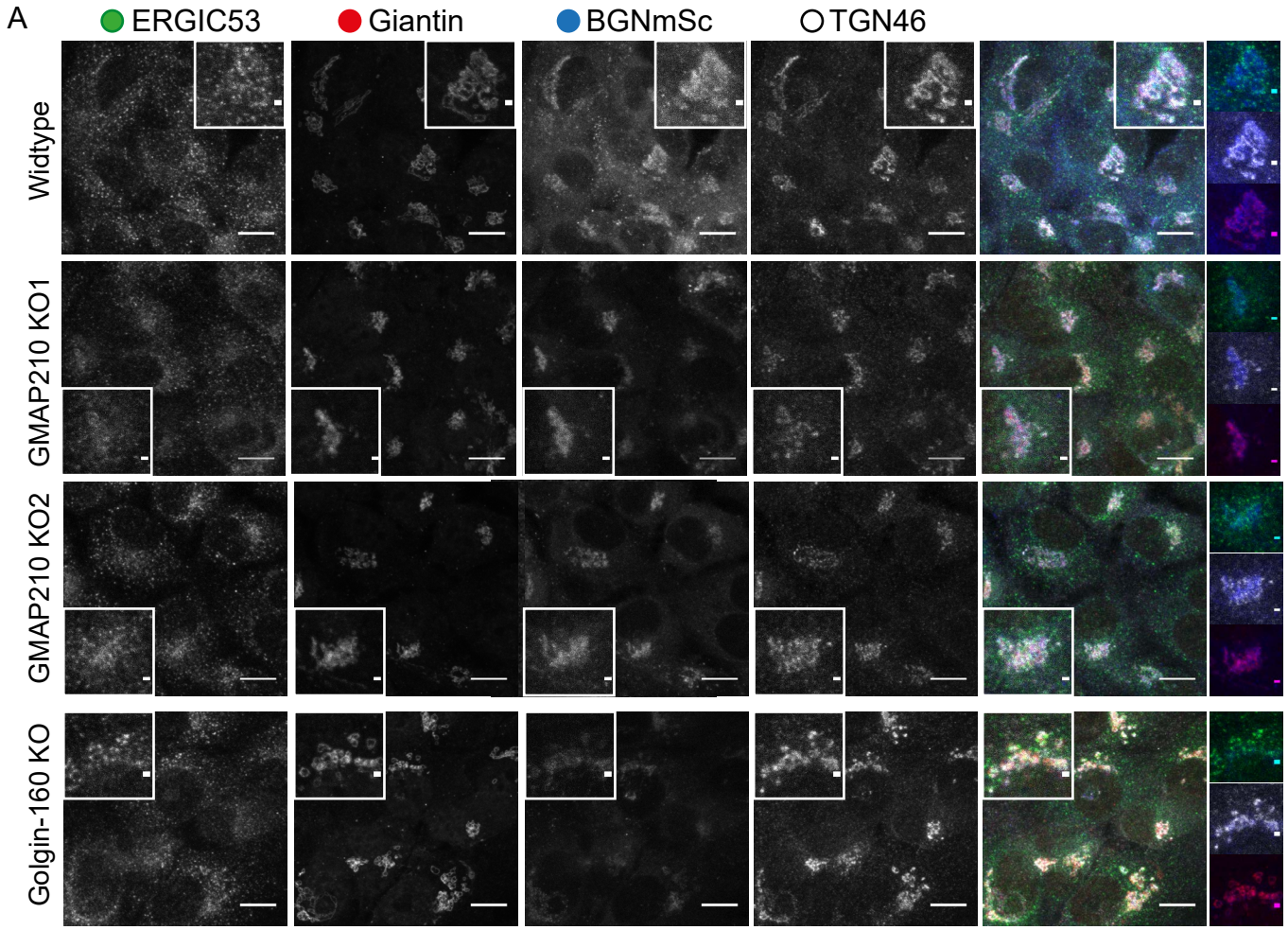
Supplemental Figure 5